Electrophoretic Deposition of Hydroxyapatite Incorporated Composite Coatings on Metallic Substrates: A Review of the Fundamentals

Sandeep Singh, Gurpreet Singh, and Niraj Bala

Abstract The electrophoretic deposition (EPD) of hydroxyapatite (HA) ceramic material is an effective strategy for a wide range of biomedical applications. This review chapter encompasses an overview of the fundamental and technical aspects of EPD approach, factors influencing the deposition process, suspension preparation, control of suspension mechanism, and deposition of composite coatings obtained by EPD. This review comprehensively analyzes the kinetics involved in EPD of HA-reinforced coatings, and the different factors such as applied voltage and deposition time, which can influence the surface morphology, corrosion behavior and in vitro bioactivity assessment. The parameters are described based on the up-to-date detailed overview of the recent research development in the area of EPD coated HA composite coatings on various metallic substrates.

1 Introduction

EPD is a promising technique for colloidal coating processes. Figure 1 represents a schematic mechanism of an EPD unit. Under the effect of electric field, the charged particles dispersed in a fluid travel toward the electrode and deposit [1, 2]. Based on surface charge, two forms of EPD can be described. If the particles are positively charged, they will be attracted to the cathode, and the mechanism is known as cathodic EPD. On the other hand, if the particles are negatively charged, they will be attracted

S. Singh (✉) · G. Singh
Department of Mechanical Engineering, Punjabi University, Patiala, Punjab, India
e-mail: sandeep_me@pbi.ac.in

N. Bala
Department of Entrepreneurship Development and Industrial Coordination, National Institute of Technical Teachers Training and Research, Chandigarh 160019, India
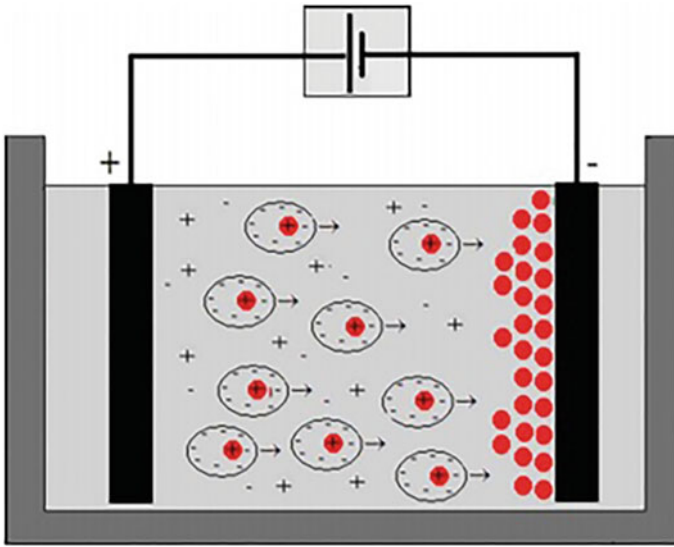
Fig. 1 Schematic diagram of EPD of charged particles with electrodes. Reprinted from Ma et al. [4], with permission from Elsevier. Copyright (2018)

to the anode and this mechanism is called anodic EPD. A current will flow between the electrodes under the application of a potential (Fig. 1). The current magnitude that flows is affected by the number of parameters, such as the solution conductivity, electrochemical kinetics and the cell constant. The suspension electric field strength (E) is analogous to the current density (J) and the suspension conductivity (k), and these three parameters are represented by Ohm's law (J = kE) [3].

Basic EPD is developed from organic suspensions which have many advantages like suspension chemical stability, low conductivity, and avoidance of the electrochemical reactions. This contributes to the formation of better quality coatings. However, the use of organic solvents is combined with several problems such as volatility, cost, flammability, and toxicity. Additionally, an organic solvent has less dissociation energy; this produces a limited particle charge density. Therefore, high electric field strengths are needed to transfer the particles toward the electrode [5].

The main application of EPD in the field of biomaterials has been the production of HA coatings on metallic substrates, where scientists intend to improve the bioactivity of surfaces and thereby facilitate the implants integration through surrounding tissues. As the main component of bone, HA demonstrates prominent osteoconductivity and biocompatibility [6], and has been extensively studied as effective a coating for bio-implants. It is easy to regulate the deposited HA thickness and stoichiometry over a broad range through EPD by adjusting processing parameters such as voltage, time and concentration. However, HA coatings are typically subjected to cracking during sintering process [7]. It was documented that implants failure occurs due to the increased degradation rate of HA coating, which decreases the implant's long-term

stability in the body environment [8]. Palanivelu et al. [9] reported that the HA-reinforced coatings have a better ability to increase the implant's life relative to the pure HA coating. In order to refine the HA coating properties, various incorporations had been analyzed in combination with polymer and ceramic phases like zinc oxide [10], silica [11], iron oxide [12], titanium oxide [13], polylactide [14], chitosan [15], and polycaprolactide [16]. In this chapter, we have considered the benefits of EPD processing, the specific and adaptive biological functions of HA, and the HA composite coatings incorporated on different substrates. Specific attention is paid to discuss the effects of particular EPD parameters such as voltage, and deposition time on surface morphology, corrosion resistance, and in vitro bioactivity of HA composite coatings.

2 Effects of EPD Parameters on Coatings

The EPD process works on the principle of electrophoresis mechanism in which the movement of charged particles starts between the electrodes due to the effect of the applied electric field. The EPD method involves two types of group parameters: (a) suspension parameters (such as particle size, suspension conductivity, viscosity, and zeta potential), and (b) process parameters (such as voltage, time). The effects of these parameters are discussed in detail in the following sub-sections.

2.1 Suspension Parameters

Numerous parameters should be considered to understand the suspension properties such as powder surface properties, additive concentration (mainly dispersant), the influence of the type of additives, and physio-chemical nature of both liquid medium and suspended particles.

2.1.1 Particle Size

To mention the relevant particle sizes for EPD, there was no general thumb rule. The primary issue with greater sizes is that the particles contribute to sediment due to the gravitational forces resulting in thick deposits in vertical cells at the base, and thin films on top. Similarly, very fine particles tend to aggregate and thus produce non-uniform deposits [17].

2.1.2 Suspension Conductivity

In EPD experiments, the conductivity of suspension plays a vital role. It has been reported that the motion of particles was low if the conductivity is too high [18]. On the other hand, the stability of particles was lost if the suspension was too resistive, because of the electronically charged particles. The conductivity increases by enhancing the applied current in the suspension [18]. It is necessary that the conductivity lies within the suitable range for the successful assessment of the EPD process.

2.1.3 Suspension Viscosity

To examine the dispersion rate, the viscosity property cannot be considered due to the negligible use of solid particles for the EPD process [19]. However, low conductivity, high dielectric constant, and low viscosity are some of the desired properties for suspension stability.

2.1.4 Zeta Potential

In the EPD process, the zeta potential plays a pivotal role in acquiring a uniform charge of suspended particles. The different role of zeta potential in the fabrication of coating is as follow: (a) Determining the superficial behavior of powder when suspended in aqueous media. (b) Determining the movement and direction of particles in suspension. (c) Resolving the interaction between particles by stabilization of the suspension [20].

2.1.5 Suspension Stability

Electrophoresis is the occurrence of particles motion in a colloidal solution under the effect of an electric field. There are generally two types of colloidal particles in suspension. Firstly, the particles having sizes of 1 μm or less in diameter, where these particles sustain in suspension for a longer period due to Brownian effect only [21]. Secondly, particles having sizes more than 1 μm, where the hydrodynamic agitation is required. The two major factors which characterize the suspension stability are settling rate and aptness to undergo flocculation [22]. Mori et al. [23] reported that the suspension was not stable until it shows no tendency to; flocculate, make adhering deposit, and settle down slowly at the bottom of the container.

Fig. 2 Weight of deposited coating (hydroxyapatite on Ti-6Al-4V substrate) versus the applied voltage for different periods: **a** 30 s, and **b** 120 s. Reprinted from Besra and Liu [29], with permission from Elsevier. Copyright (2007)
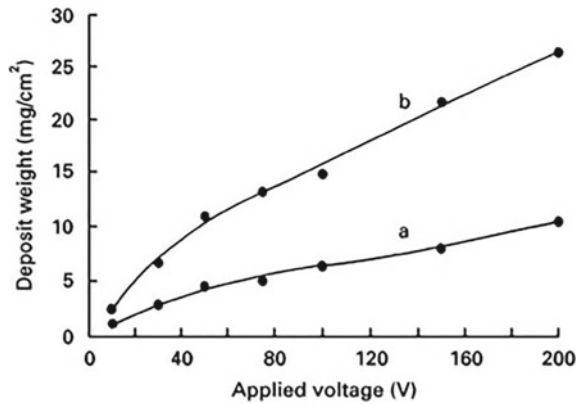
2.2 Process Parameters

2.2.1 Effects of Applied Voltage

In the EPD process, it is generally considered that the increase in applied voltage enhances the amount of deposition. However, higher voltage leads to film roughness [24], wrinkling, bubble formation, heterogeneity in the surface of the coating, and generates porosity [25]. Figure 2 depicts the deposition of HA coating on Ti-6Al-4V substrate. It was observed that the weight deposited increases by enhancing the applied voltage, but it can also affect the quality of the coating. Basu et al. [26] reported that the film deposited was more uniform, at a potential in the range (25–60) V/cm, whereas the crack occurs in the coating if the applied voltage was more than 60 V/cm. The non-uniformity of film originates at high voltage due to the anisotropy of the electric field on the substrate. Due to this reason, the deposition of particles takes place at the edges [27] of electrodes and generates aggregates in suspension [28].

It should also be noticed that too low voltage will not improve the film quality. On the other hand, more increase in applied voltage leads to the formation of the porous structure. Tabesh et al. [30] analyzed the porosity increase for HA-reinforced composite coatings by increasing the voltage from 5 to 40 V/cm, and concluded that the applied voltage plays an important role in the porosity of deposited composite coatings.

2.2.2 Effect of Deposition Time

The microstructure of electrophoretically deposited HA composite coatings is also affected by another important parameter, i.e., deposition time [31–33]. Karimi et al. [34] reported that the surface roughness of HA films enhanced with longer deposition time due to the agglomeration of particles in suspension. Similarly, in the earlier

Fig. 3 Current density against deposition time of HA coating at different voltages **a** 10 V; **b** 20 V; **c** 30 V. Reprinted from Besra and Liu [29], with permission from Elsevier. Copyright (2007)
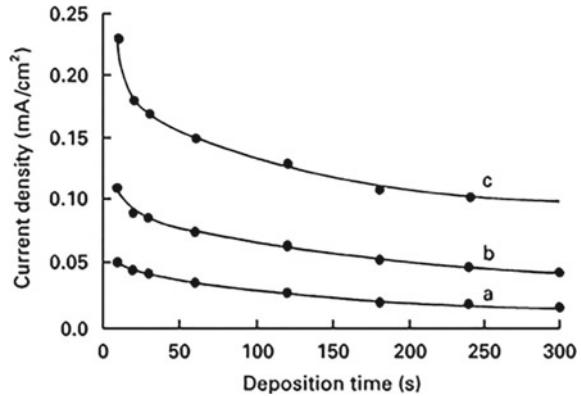
studies [35, 36] it was also observed that the non-uniform thick layer and porosity occurred on the surface of the substrate with longer deposition time.

From Fig. 3 it was revealed that at a constant voltage EPD, the effect of electric field on electrophoresis decreases with an increase in the deposition time due to the generation of particles insulating layer on the surface of electrodes. But during the starting phase of the process, the relationship between mass deposition and time was linear.

2.2.3 Effects of Gap Between Electrodes

The gap between electrodes plays an important role in the electrophoretic deposition process. If the gap is too large there were no depositions due to the resistance offered by an electrolyte. On the other hand, if the gap was too small, there were inconveniences to a current flow in the electrolyte. Based on Table 1, many of the researcher's maintain a gap within the range of 10–20 mm between the main and counter electrode [37]. The use of counter electrode in the EPD process provides potential to the working electrode within the suspension medium. To keep the counter electrode dissolving in suspension medium it is usually made of inert material such as graphite on noble metal [38].

2.2.4 Effects of Post-EPD Treatment

For post-EPD treatment of HA-reinforced coatings, different results have been reported by various researchers. The earlier studies on HA composite coatings have shown that the heat treatment leads to surface smoothing, compaction, and reduction of the interlayer spacing between the coating and substrate by removing the trapped water molecules. In addition, the formation of crevices [39], flaky surfaces, and protruding composite coating edges are also outcomes of post-EPD treatment.

Table 1 Chronological summary of recent studies (2007–2020) of HA-based composite coatings fabricated by EPD and brief description of their surface properties

Sr. no	Year	HA-reinforced matrix	Substrate	Voltage (V) and time (min)	SEM[1] morphology	Corrosion behavior	In vitro bioactivity assessment	References
1	2007	HA-BG[2]	Ti-6Al-4V	30–75, 2–10	The coating performed at 30 V and 5 min was found to be optimum and homogeneous	–	–	[44]
2	2008	HA-BG	Ti-6Al-4V	30–90, 2–5	Spherical particles of HA and BG consist of great number of agglomerated nanosized needle-like sub-particles	Current density of coated sample was reduced to 0.22 A/cm^2 to from 0.32 A/cm^2 for the uncoated sample	–	[45]
3	2009	HA-BG-CS-Alginate[3]	Pure Ti	10–30, 10	Uniform and crack free	–	–	[46]
4	2009	HA	Ti-6Al-4V	20, 30	Less uniform with micropores	Coated sample has 40% more corrosion rate than Ti-6Al-4V	Apatite formation after 4 weeks in Hank's solution	[47]
5	2010	HA-CNTs[4]	Ti-6Al-4V	2 mA, 8 s	No microcracks but rougher surface was observed at higher content of CNTs	Current density of coated sample (HA-10% of CNTs) declined to 0.15 $\mu A/cm^2$ compared to 8 $\mu A/cm^2$ of uncoated sample	After 3 weeks of immersion in SBF[5] apatite was formed on the entire surface of coated samples	[48]
6	2010	HA-CNTs 2010	Ti	10–40, 0.5–8	Thick coating free of cracks obtained at 20 V	Coated samples at 20 V have lower current density	CNTs surface can act as nucleation sites resulting in the formation of HA layer	[49]
7	2011	HA-TiO$_2$ 2011	Ti	165, 5	Increasing HA concentration leads to less micropores structure	Least current density (1.786×10^{-7} A/cm^2) at HA concentration (5 g/L)	Spheroid shape apatite crystallized form on HA surface after 6 days immersion in SBF	[50]

(continued)

Table 1 (continued)

Sr. no	Year	HA-reinforced matrix	Substrate	Voltage (V) and time (min)	SEM[1] morphology	Corrosion behavior	In vitro bioactivity assessment	References
8	2011	HA 2011	Ti	20–140, 1–7	At low voltage (20 and 30 V) no cracks and surface was found to be uniform	–	–	[51]
9	2012	HA-TiO$_2$ 2012	Ti-13Nb-13Zr	30, 5	Densely packed with less porosity	Declined by one order of magnitude	–	[52]
10	2012	HA-MgO 2012	AZ31 Mg	140–550, 5	Composite coating has less porosity at low voltage than at higher voltage	Current density decreased one fold of order (2.25×10^{-3} to 7.76×10^{-4})	Bioactivity improved at pH value 4.5	[53]
11	2012	HA 2012	NiTi alloy	40–80, 2	60 V results in dense, uniform pores formation at 80 V	–	Surface covered with apatite crystals after 1 week of immersion in SBF	[54]
12	2013	n-HA	AZ91 Mg alloy	30, 5	Formation of dense and uniform HA layer	C.R. of coated sample was 48.2% more than the uncoated sample	Bone-like apatite crystals formed after immersion in SBF	[55]
13	2013	n-HA	AZ91 Mg alloy	50, 15	Almost crack free and homogeneous coatings	Current density reduced to 2.21 µA/cm^2 from 22.14 µA/cm^2	Apatite formation due to the creation of nucleation sites	[56]
14	2013	HA	AZ31 Mg alloy	10–30, 20	Fairly uniform coating at 10 V	corrosion of coated sample decreased to 9×10^{-6} A/cm^2 from 1.2×10^{-4} A/cm^2	–	[57]
15	2013	HA-MgO 2013	Pure Ti	0.85 mA, 20–30	Smooth and dense	C.R. of coated sample 14% higher than the Ti sample	Spherical apatite formation after 5 days immersion in SBF	[58]

(continued)

Table 1 (continued)

Sr. no	Year	HA-reinforced matrix	Substrate	Voltage (V) and time (min)	SEM[1] morphology	Corrosion behavior	In vitro bioactivity assessment	References
16	2013	HA coat on Ti-CaP composite coating 2013	Ti	10, 6	CaP particles are distributed uniformly in the Ti matrix	C.R. of coated sample was 56% higher than the Ti sample	–	[59]
17	2014	HA-GO [6] 2014	Pure Ti	30, 1–5	Minor cracks in pure HA but filled by addition of GO	Current density declined by two folds of magnitude than pure Ti	Presence of GO fillers promotes the bioactivity and cell proliferation	[60]
18	2014	HA 2014	Pure Ti	10—40, 2	Porous HA coating with no observable cracks	–	Bioactivity enhanced by the combined effect of crystallinity and Ca^{2+} content of the surface	[61]
19	2014	HA-PEG[7] 2014	316L SS	30, 10	Uniformly distributed and homogeneous	Effectively improve the passive ability of 316L SS	Potentially enhance bioactivity and induce implant osteointegration with living cells of human	[62]
20	2015	HA-Gr[8] 2015	Ti	60, 2	Fewer microcracks on composite coating compared to pure HA coating	HA-Gr coating has superior C.R. than its pure HA counterpart	enhanced precipitation of a newly formed apatite layer with more concentration of Gr in HA coating	[63]
21	2015	HA-BG-CS 2015	Pure Ti	20, 10	Smooth distribution of HA, BG particles along with CS molecules	Current density of coated sample reduced to 0.073 from 10.5 (μm/cm^2)	Higher bioactivity at pH value 3.3 as compared to pH value 4.5 and 5.0	[64]
22	2015	FHA[9]	AZ91 Mg alloy	100, 3	FHA coating is rough and porous with net-like surface structure	Current density of coated sample reduced to 12.5 from 63,1000 (nA/cm^2)	Spherical apatite formation after 2 weeks after immersion in SBF	[65]

Table 1 (continued)

Sr. no	Year	HA-reinforced matrix	Substrate	Voltage (V) and time (min)	SEM[1] morphology	Corrosion behavior	In vitro bioactivity assessment	References
23	2015	HA-BG 2015	Pure Ti	30, 2	Rough microstructure contains micropores	Current density decreased by one fold of magnitude (from 2.76 to 0.27 µA/cm^2)	Required time for apatite formation of HA-BG composite coating less than the pure HA coating	[66]
24	2015	HA 2015	Ti-6Al-4V	5–20, 5–20	Homogeneous structure at 10 V compared to 15 and 20 V which contributes to heterogeneous and porous structure	–	–	[67]
25	2015	HA-Mg 2015	Ti-6Al-4V	10, 5	Micropores observed on needle and plate like morphology	C.R. of coated sample with least content of Mg was 70% more than Ti-6Al-4V sample	After 7 days immersion in SBF, samples were covered with newly grown apatite layer	[68]
26	2016	HA-BG-CS-HAL[10] 2016	Pure Ti	30, 10	Spherical morphology with the presence of cracks and porosity	Corrosion current density diminished from (91 to 0.56 µA/cm^2)	Bioactivity improves due to unique properties of HAl like augmenting drug delivery	[69]
27	2016	CS 2016	Ti-13Nb-13Zr	5–30, 4	Homogeneous coating at 10 V	Corrosion passivation of coated sample was more than uncoated sample	–	[70]
28	2016	HA 2016	Mg-3Zn alloy	20, 10	Fewer cracks observed for sample annealed at 300 °C than 400 °C	C.R. improved up to an impressive 25 times than Mg alloy	Fast apatite nucleation of HA coating due to similarity in crystal structure than Mg	[71]
29	2016	HA 2016	WE43Mg	30, 10	Formation of thick and porous coating	Current density declined to (0.090 mA/cm^2)	–	[72]

(continued)

Table 1 (continued)

Sr. no	Year	HA-reinforced matrix	Substrate	Voltage (V) and time (min)	SEM[1] morphology	Corrosion behavior	In vitro bioactivity assessment	References
30	2017	HA-MgP-ZnP 2017	AZ31 Mg	20, 10	Compact and dense uniform appearance	Current density decreased by 6 order of magnitude than AZ31 Mg sample	After 21 days of immersion least rate of corrosion due to formation of fully apatite layer	[73]
31	2017	HA-CS 2017	Ti-13Nb-13Zr	8–20, 1–6	Homogeneous and continuous coating at 10 V whereas pores were observed at 20 V	Current density reduced from 20 $\mu A/cm^2$ for the uncoated sample to 6 $\mu A/cm^2$ for the coated sample	Creation of cauliflower-like hydroxyapatite deposits on the surface of coated samples	[74]
32	2017	HA-Zn-Silk Fibron 2017	Pure Ti	30, 10	Uniform, homogeneous surface and free from microcracks	Better corrosion protection with coating than uncoated sample	After 3 days of immersion new apatite layer with rod shaped crystals covered all surface of samples	[75]
33		HA-Cu	Ti-13Nb-13Zr	30, 1–2	Inhomogeneous and several HA agglomerates at 1 min time whereas more homogenous at 2 min time	–	Increase of Cu nanoparticles decreased the bioactivity	[76]
34	2018	TiO$_2$-MAO-Zn-HA[11] 2018	Mg alloy	15, 60	Large number of pores on TiO$_2$ doped MAO sample and few agglomerates of fine particles on ZH[12] coating	Current density of ZH coating was declined to 1.2 ± 0.3 $\mu A/cm^2$ compared to Mg alloy	Agglomeration of the apatite with spherical morphology has found	[77]
35	2018	HA-CS-COL[13]-h-BN[14] 2018	Ti-6Al-4V	15, 5	Creation of pores due to collagen orientation	Corrosion current density of coated samples reduced by two order of magnitude than uncoated sample	Synergetic effect of collagen leads to the formation of nucleation sites	[78]

(continued)

Table 1 (continued)

Sr. no	Year	HA-reinforced matrix	Substrate	Voltage (V) and time (min)	SEM[(1)] morphology	Corrosion behavior	In vitro bioactivity assessment	References
36	2019	HA-CS-GO 2019	Ti	30, 3	Spherical agglomerates of HA particles form clusters	current density of 21 nA/cm^2 significantly lower than that of the Ti about 200 nA/cm^2	Oxygenic functional group of GO nanosheets helps to improve the bioactivity	[34]
37	2020	HA	ZK60 Mg alloy	100, 10	Spherical closely linked agglomerates of HA particles	HA coating on ZK60 reduced the current density by one order of magnitude and resulted in more than five times lower uniform corrosion rate	–	[79]
38	2020	HA-BG-CS-HNT[(15)] 2020	Ti	10–50, 5–25	Formation of cracks and porosity at higher voltage and deposition time	Least current density of coated sample at 30 V which was reduced to 0.578 μA/cm^2 from 91.2 μA/cm^2 of Ti sample	Silanol functional group (Si–O–Si) of BG can induce the spherical apatite formation	[80]
39	2020	HA-Zein 2020	316L SS	6–15, 3–9	Homogeneous porous film was observed at 15 V and 3 min	Current density of 316L SS was 0.32 μA/cm^2 and declined to 0.046 μA/cm^2	Formation of HA crystals after 3 days of immersion in SBF	[81]
40	2020	HA	ZMX410 and ZM21 Mg alloys	37, 5	Observed homogeneity and uniformity of the HA coating on both alloys	Corrosive protection efficiency by HA coating to ZM21 and ZMX410 was 40.6% and 4.42% respectively	Coated samples were hydrophilic and bioactive in nature and generate apatite layer after immersion in SBF solution	[82]

[(1)] SEM: Scanning electron microscope; [(2)] BG: Bioglass; [(3)] CS: Chitosan; [(4)] CNT: Carbon nanotube; [(5)] PEG: poly(ethylene glycol); [(6)] GO: Graphene oxide; [(7)] PEG: poly(ethylene glycol); [(8)] Gr: Graphene; [(9)] FHA: Fluoridated hydroxyapatite; [(10)] HAL: Halloysite; [(11)] MAO: Micro-arc oxidation; [(12)] ZH: Zinc-doped hydroxyapatite; [(13)] COL: Collagen; [(14)] h-BN: Hexagonal boron nitride; HNT: [(15)] Halloysite nanotube

However, at high temperature (above 1200 °C), the dimensions of the substrate change, and the result is shrinkage of the coating [40]. Therefore cracks occur in the coating. During the cooling process, additional cracking occurs due to the difference between thermal expansion coefficients of the sintered coating and the substrates. Other problems that occur at high temperatures are oxidation and phase transformations between the coatings and substrate [41]. These problems can be eliminated by selecting a suitable range of temperatures (550–800) °C for post-EPD treatments [42]. Another alternative to avoid these troubles is by the development of inorganic-polymer composite coatings. The use of polymer involves processing at low temperature and avoiding the inconvenience of heat treatment process [43].

3 EPD on Metallic Substrates with Hydroxyapatite Reinforced Composite Coatings

Table 1 lists a chronological summary of recent studies (2007–2020) of HA-based composite coatings fabricated by EPD and brief description of their surface properties such as surface morphology, corrosion behavior [in terms of corrosion current density (I_{corr}) and corrosion potential (E_{corr})] and bioactivity assessment. From the analysis of the literature review it was observed that different parameters such as voltage, deposition time can influence the surface properties of HA-reinforced composite coatings which are discussed below:

The discussion of Table 1 on coating structure, corrosion behavior and in vitro bioactivity results obtained for HA-based coatings developed by EPD.

Stojanovic et al. [44] developed the HA coating on Ti-6Al-4V alloy using EPD. HA particles suspension was formulated by the stirring of 0.5 g of HA in 100 ml ethanol. The effect of EPD parameters, i.e., voltage (30, 50 and 75 V) and time (2, 5 and 10 min) on coating morphology and deposited weight were determined. It was observed that raising the applied voltage leads to more deposition yields. Figure 4 shows the relationship of the deposited weight against time and voltage.

The coating was performed at 30 V and 5 min and was found to be optimal compared to 50 and 75 V. It was found that although the coating thickness was enhanced at higher voltage, cracks formed in the coating. Figure 5 depicts the surface morphology of coatings developed by EPD at 30 and 50 V. Therefore, it was concluded that by regulating the voltage and time, the weight and thickness of coating can be controlled.

Balamurugan et al. [45] formulated a BG-HA composite coating on Ti-6Al-4V by EPD. The prepared coatings have been characterized for their structural and electrochemical properties. The coatings produced at 20 V contributed to irregular coatings, while the coatings processed for 70 V and 5 min were thicker and extremely porous. The possible mechanism is a spontaneous deposition of particles that are loosely packed and isolated by a more volume fraction of porosity, resulting in
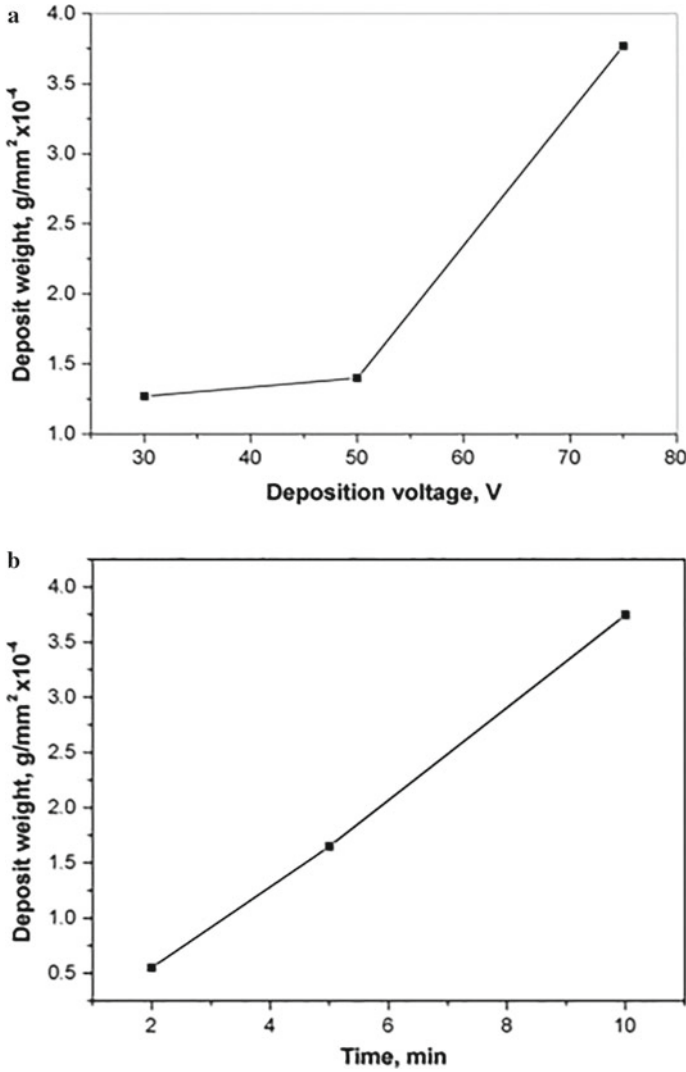
Fig. 4 a Dependence of deposited coating weight on deposition voltage at constant time of 10 min. **b** Dependence of deposited coating weight on time at a voltage of 75 V and **c** Dependence of deposited coating weight on time at constant voltage of 30 V. Reprinted after Stojanovic et al. [44], with permission from Elsevier. Copyright (2007)

the formation of inter-particle cracks and eventual detachment of particles from the substrate. The E_{corr} and I_{corr} for Ti-6Al-4V were −0.97 V and + 0.32 A/cm^2, respectively. For HA, bioglass (BG), and BG-HA-coated samples under 70 V for 5 min, the E_{corr} values were observed to be (0.325 ± 0.5) V, (0.380 ± 0.5) V, and (0.475 ± 0.5) V, while the values of I_{corr} were 0.60, 0.33, and 0.22 A/cm^2,
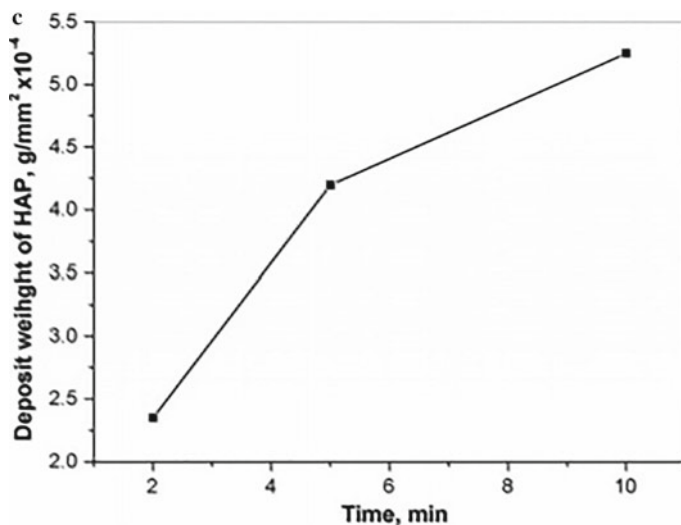
Fig. 4 (continued)
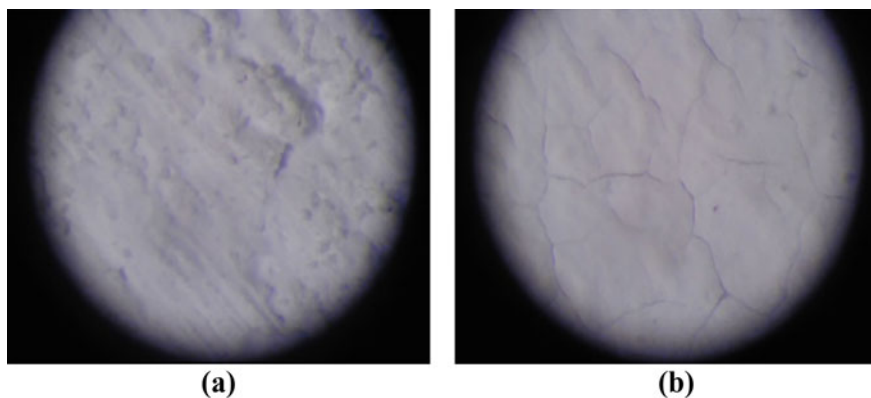
Fig. 5 a Coating obtained by EPD at 75 V and 10 min, and **b** coating obtained by EPD at 30 V and 5 min. Reprinted after Stojanovic et al. [44], with permission from Elsevier. Copyright (2007)

respectively. However, the E_{corr} of BG-HA-coated samples at 30 V, 50 V, 60 V, and 90 V persisted at (0.171 ± 0.5), (0.264 ± 0.5) V, (0.410 ± 0.5) V, and (0.388 ± 0.5) V, implying that the optimum coating potential varies from 50 to 70 V. The E_{corr} for all the coated samples was observed to be more noble relative to the Ti-6Al-4V, thus demonstrating improved corrosion resistance.

Zhitomirsky et al. [46] investigated the fabrication of BG-HA-CS and BG-HA-alginate coatings by EPD. EPD was performed at (10–30 V) in an electrolyte containing 0–2 g/L BG and 0–1 g/L HA. Coatings performed at 10 V were uniform

and crack free, however porous structure observed at 30 V. Due to the use of poly-mers like chitosan (CS) and alginate, problems related to the sintering of BG and HA coatings on the metallic substrate are avoided. In addition, ambient temperature processing allows the integration of other functional materials as reinforcements into the coatings. The examples are signaling of cell biomolecules or antibiotic agents may be applied to the polymer and thereby homogeneously integrated into the polymer matrix.

Kwok et al. [47] fabricated HA coatings with and without carbon nanotubes (CNTs) on Ti-6Al-4V. The corrosion and in vitro bioactivity properties of the HA-coated specimens were evaluated. The coating was crack free having 10 μm thick-ness, and deposited at 200 V for 30 min. The coated samples were more resistant to corrosion than the substrate. This enhancement was endorsed by a noble shift in the corrosion potential and a lower I_{corr}. Besides, after soaked in Hanks' solution for 4 weeks apatite was formed on the HA coatings, showing high bone bioactivity.

Zhang et al. [48] developed HA coating with different concentrations of CNTs (4–25%) by EPD on Ti-6Al-4V substrate to increase the bone bioactivity and osteoin-tegration with metallic implants. Cathodic EPD was performed under a current of 2 mA and deposition time of 8 s. No cracks were observed on the surface of coated samples with 10% of CNTs. As the content of CNTs increased, cracks and pores were observed, which leads to decline in the corrosion rate. Among the coated samples, the HA-10% CNTs coating possessed the highest corrosion resistance and prominent bone bonding ability.

Bai et al. [49] synthesized carbon nanotube-hydroxyapatite (CNT-HA) compos-ites by chemical method before an EPD process. EPD was performed at 10, 20, and 40 V, and the deposition time varied from 0.5 to 8 min.

The surface morphologies of the CNTs–HA coatings appeared similar and contain micropores. The coating thickness was 10, 18, and 34 μm at 10, 20, and 40 V. The morphology was alike at different voltages, however, the low magnification micrographs reveal that the morphologies were actually different. At 40 V, the coat-ings have more cracks, relative to the lower voltages (i.e., 10 and 20 V). The crack formation at a high voltage occurs due to the evolution of hydrogen at the cathode. Figure 6 compares the surface morphologies at higher and lower magnification obtained at different voltages. Therefore, it was concluded that crack free coatings were attained at a voltage of 20 V, which provide effective corrosion protection and good biocompatibility.

Bai et al. [50] fabricated HA-TiO$_2$ coating on Ti by micro-arc oxidation (MAO) combined with EPD with various amounts of HA particles. The EPD was conducted at 165 V for 5 min. Without the incorporation of HA particles to the electrolyte, the samples exhibited a rough and porous TiO$_2$ layer developed by MAO on the surface of Ti. Figure 7 shows the surface morphology at different concentrations of HA particles. It was found that the samples produced at lower HA concentration contain a number of pores.

The coating surface was less porous as the concentration of HA raised to 20 g/L. The sample developed at 5 g/L HA concentration revealed the highest corrosion resistance and better formation of apatite layer over the entire surface.

High Magnification   **Low Magnification**
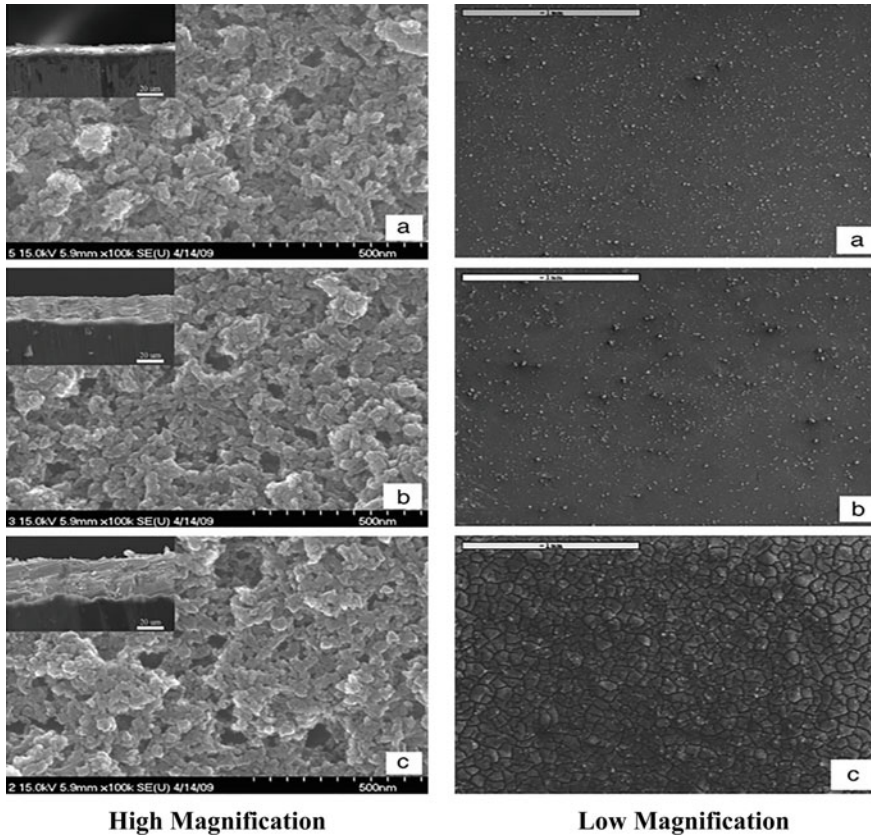
Fig. 6 Scanning electron microscope (SEM) images of the CNTs-HA coatings produced at 8 min duration with voltages: **a** 10 V; **b** 20 V, and **c** 40 V. Reprinted from Bai et al. [49], with permission from Elsevier. Copyright (2010)

Abdeltawab et al. [51] produced HA coating on Ti substrate by EPD. The effect of applied voltage (20–140 V) and time on deposition rate, thickness, and structure of coating were studied. From the analysis of results, authors observed that, at higher applied field, turbulence takes place in the suspension and the deposition process may be affected by the flow disturbance in the surrounding medium. The reason may be the fast movement of particles in the suspension as they cannot get adequate time to find the appropriate positions to develop a close-packed structure. Figure 8 depicts the weight of the deposit, and the thickness as a function of applied voltage.

Although powders may be deposited rapidly if larger applied fields are used, the performance of the deposit can be affected. The particle size increases with more applied voltage as observed from the SEM images of Fig. 9. No cracks were detected at 20 and 30 V voltage, and the coating was found to be smooth. Nonetheless, marginally larger particles have been found in coatings processed at 40 and 60 V
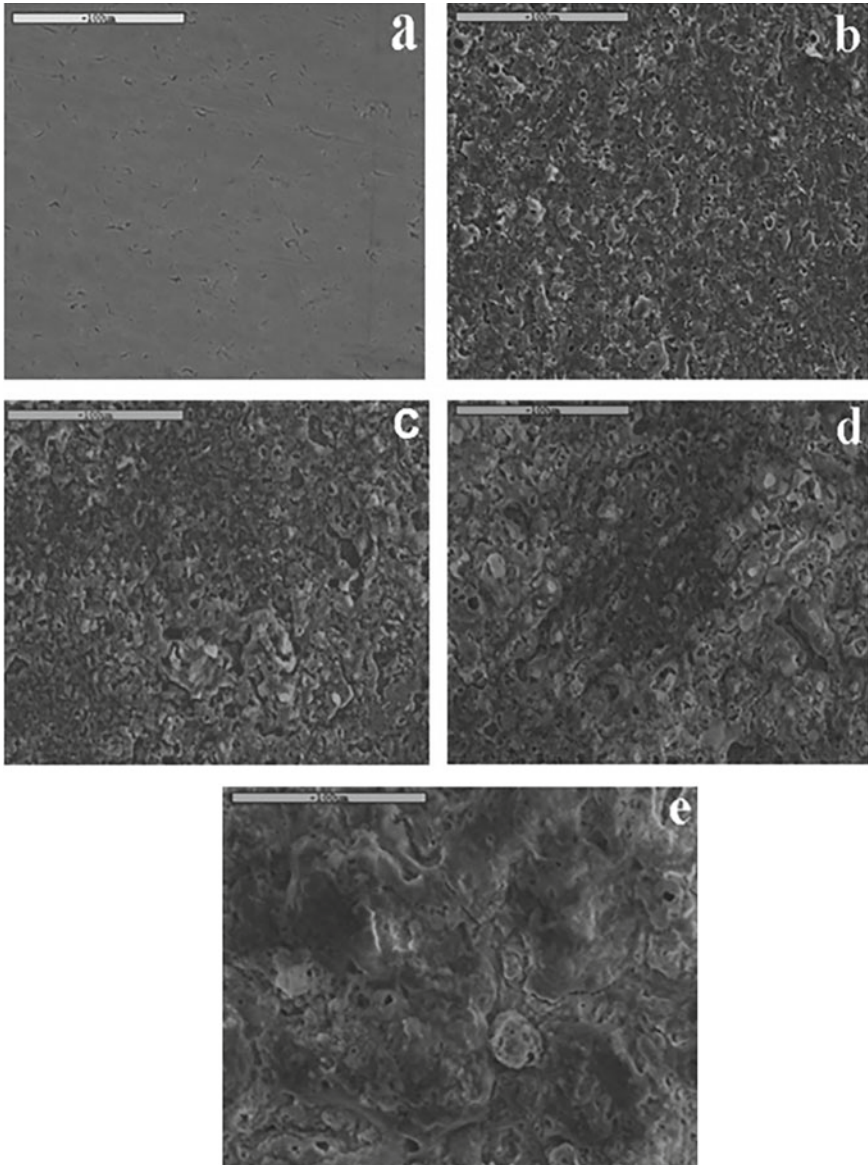
Fig. 7 Surface morphology of Ti (**a**), and coated samples with HA concentration of **b** 0 g/L, **c** 5 g/L, **d** 10 g/L, and **e** 20 g/L. Reprinted from Bai et al. [50], with permission from Elsevier. Copyright (2011)
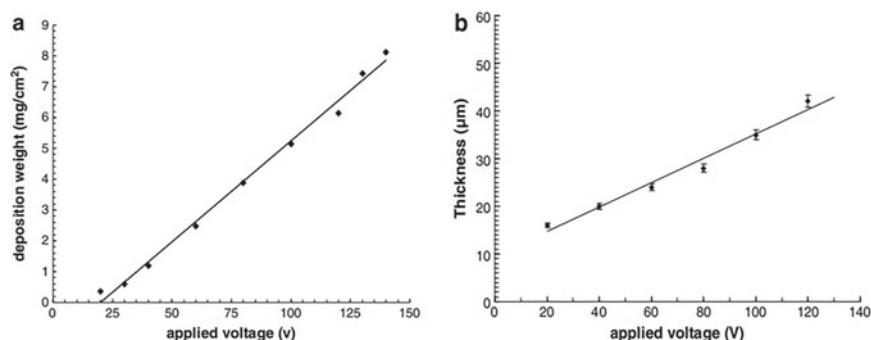
Fig. 8 **a** Weight of HA deposited, and **b** HA coating thickness versus voltage at constant time duration 5 min. Reprinted from Abdeltawab et al. [51], with permission from Elsevier. Copyright (2011)

voltages. Besides, small cracks (40 V) and some larger cracks (60 V) were detected on the surface of coatings.

Mohan et al. [52] investigated the corrosion behavior of TiO_2 + 50% HA-coated Ti-13Nb-13Zr alloy. A thin coating was attained by EPD at 30 V followed by sintering at 850 °C. The microstructures of the sintered and unsintered samples were evaluated by optical microscopy. The SEM-EDAX results exhibited that the sample sintered at 850 °C was densely packed. The unsintered coating exhibited a large number of partially bonded composite particles. The HA-TiO_2 sample depicted a lower corrosion rate and nobler passive potential relative to the Ti-13Nb-13Zr sample.

Sreekanth and Rameshbabu [53] developed magnesium oxide and hydroxyapatite (MgO/HA) coating on AZ31 Mg alloy to control the biodegradability rate. The coating was produced via hybrid method coupled with plasma electrolytic oxidation (PEO) and EPD. Degradation of HA coating was examined by performing electrochemical tests (pH 4.5), replicating the osteoblast resorption condition in vitro and also in the SBF environment (pH 7.4). The corrosion rate of composite coating has demonstrated a significant increase at pH 4.5. However, smaller improvement was observed at a pH of 7.4. This can be ascribed to the existence of Cl^- ions in SBF which may be accountable for corrosion at a pH of 7.4. There was also no major difference in the electrolyte pH during electrochemical testing in both 7.4 pH and 4.5 pH solutions. The analysis of results revealed that the MgO/HA coating substantially enhanced the corrosion protection of Mg alloy under both environments.

Maleki-Ghaleh et al. [54] developed HA coating on NiTi alloy via EPD. A stable suspension was made by the addition of 80 g/L HA powder to butanol. EPD was conducted at a different voltage (40, 60, and 80 V) in 120 s. It has been shown that the specimen coated at 60 V has a dense coating. Figure 10 displays the SEM morphology of HA coating at three different voltages.

As shown in Fig. 10, the coating at 60 V consists of dense and smooth coating whereas the coating at 80 V results in a coating with large pores. The findings of the SBF immersion test showed that the sample coated at 60 V performed most effectively
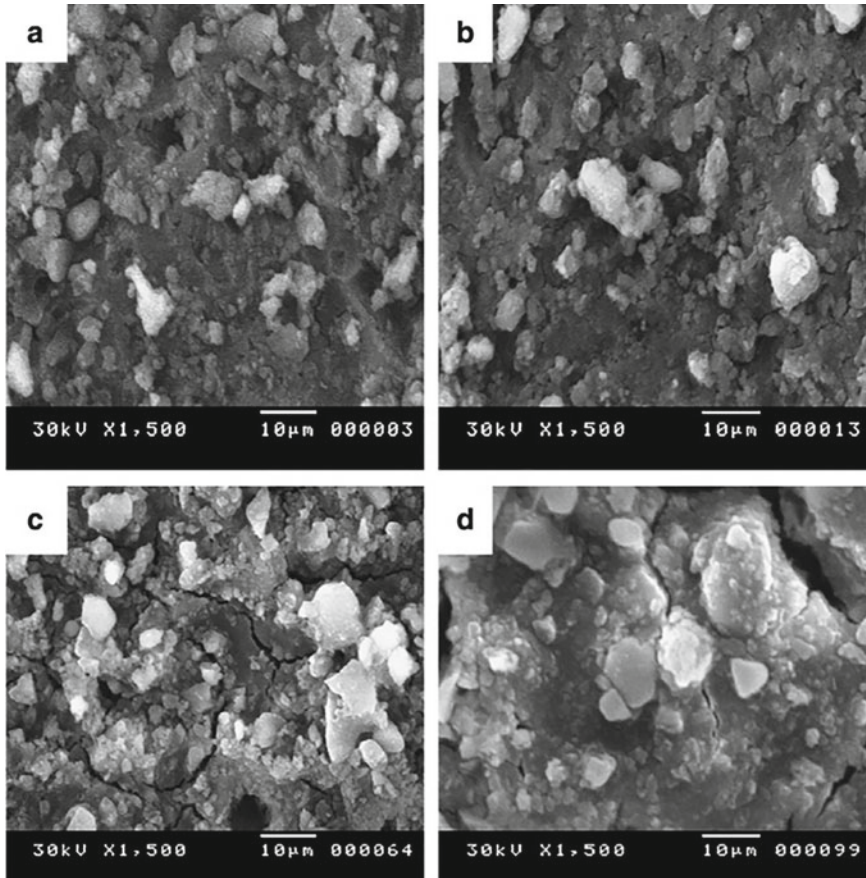
Fig. 9 SEM images of HA-coated samples at **a** 20 V, **b** 30 V, **c** 40 V, and **d** 60 V. Reprinted from Abdeltawab et al. [51], with permission from Elsevier. Copyright (2011)

and acted as a shield against the penetration of Ni ions. The uniform apatite formation on the coated surface at 60 V after one week of immersion exhibited the HA coating biocompatibility after EPD and sintering process.

Rojaee et al. [55] developed the MAO and MgF_2 as pre-surface treatments of AZ91 Mg alloy to produce a nanostructured n-HA coating. The EPD was done at 30 V for 5 min. The electrochemical tests were performed to evaluate the corrosion performance of the specimens, and in vitro bioactivity evaluation was carried out in SBF. Results have shown that the MAO/n-HA-coated samples with rough structure and reduced corrosion current density resulted in a declined degradation rate of Mg followed by high bioactivity. The presence of MgF_2 and MAO coatings could offer a strong barrier to rapid degradation of the substrate. In addition, this interlayer plays a significant role in improving the biocompatibility of Mg alloy.
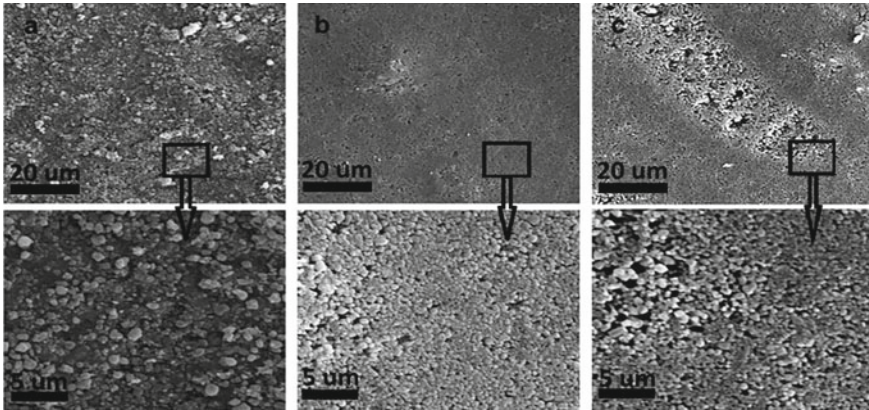
Fig. 10 SEM images at voltages of **a** 40 V, **b** 60 V, and **c** 80 V with a time duration of 120 s. Reprinted from Maleki-Ghaleh et al. [54], with permission from Elsevier. Copyright (2012)

Rojaee et al. [56] fabricated the nanostructured HA coating via sol–gel and EPD (50 V for 15 min) method on AZ91 Mg alloy. The E_{corr} of the uncoated sample was (-1448 ± 51) V. The E_{corr} values of the sol–gel and EPD produced samples were observed to be (-1343 ± 35) V and (-1406 ± 21) V, respectively. The I_{corr} of AZ91, sol–gel, and EPD coated specimens were (22.14 ± 3.21), (2.83 ± 0.04), and (2.21 ± 0.02) $\mu A/cm^2$, respectively. Generally, lower corrosion current density depicts a smaller corrosion rate. With respect to the E_{corr} and I_{corr} values, all coated specimens moved in noble directions in corrosive environments. The better corrosion protection not only monitors the Mg consumption for bone restoration, but also improves the structural integrity and cell adhesion, at the same time.

Kaabi et al. [57] synthesized hydroxyapatite (HA) coating on AZ31 substrate to alter the corrosion rate of magnesium and improve its potential applicability as implant. Coatings were deposited electrophoretically at different potentials from 10 to 30 V. The surface morphologies at different voltages are shown in Fig. 11.
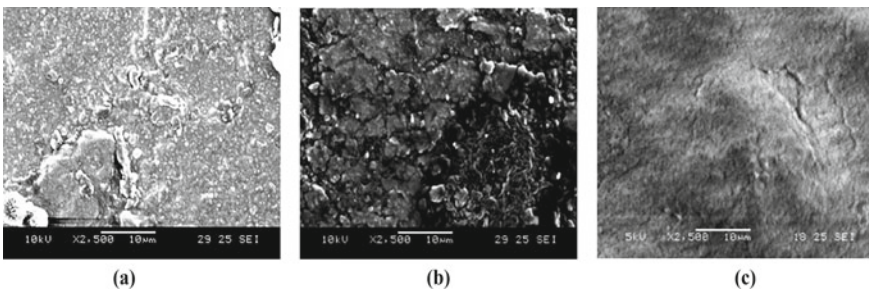
Fig. 11 SEM micrographs of (HA) coatings on AZ31 substrates at **a** 10 V, **b** 20 V, and **c** 30 V deposition potential. In all cases, the deposition time was 20 min. Reprinted from Kaabi et al. [57], with permission from Elsevier. Copyright (2014)

When the applied voltage increases, the HA particles can travel faster and accumulate quickly, thus increasing the amount of the deposit with more applied potential. There were few cracks on the HA-coated coating produced at 20 and 30 V relative to the 10 V. It was found that by enhancing voltage, the corrosion resistance was improved due to the formation of thick layer of coating.

Huang et al. [58] illustrated the corrosion behavior and bioactivity of manganese-doped hydroxyapatite (MnHAp) film on Ti. The coating was deposited at the following conditions: pH = 4.3, $I_{corr} = 0.85$ mA cm^{-2}, and 20–30 min deposition time. The MnHAp crystals consist of needle-like shape with few Mn incorporations. The inclusion of Mn^{2+} into HA substantially decreased the porosity, and the coating surface became denser. The MnHAp coating displayed more corrosion protection in SBF as compared to the HA coating. SBF immersion experiments showed that MnHAp-coated sample seemed to have better in vitro bioactivity. The addition of Mn and deficiency of Ca in the coating were the primary reasons for the superior bioactivity. The MnHAp film is a potential material to produce advanced biomedical implants.

Farnoush et al. [59] fabricated nano-HA coatings on the Ti-CaP layer by the combination of friction stir processing (FSP) and EPD. The corrosion behavior was evaluated by potentiodynamic polarization tests. By implementation of FSP, the Ti-CaP inner layer serves as a barrier to the penetration of Cl^- ions, and inhibits the electrochemical reactions between the coating and substrate. The findings referring to the HA-Ti-CaP sample suggest a substantial decline in the I_{corr}, and an improvement in the E_{corr}, and corrosion rate.

Li et al. [60] prepared homogeneous graphene oxide/hydroxyapatite (GO/HA) coating on Ti by EPD. Ethanol was used as electrolyte medium to mitigate the gases evolution at the electrodes which may have detrimental effects on the performance of the coatings. Three kinds of suspension were formulated and represented as HA, 2GO/HA, and 5GO/HA, having 0, 2, and 5 (wt. %) GO contents, respectively. EPD was executed at 30 V for 1–5 min. The rate of deposition was calculated by weight test. The deposit mass indicates a liner dependency on time, and the potential on the deposit is constant. Figure 12(a) and (b) shows the weight versus deposit time relationship at different concentrations of GO content.

As examined in Fig. 12(a), the rate of deposition declines along with the extended time of deposition, due to the development of GO/HA composite layer, which would contribute to the decrement of potential drops in the suspension. Figure 12(b) shows the inclusion of GO will decrease the HA particles deposition rate. As contrast with pure HA coating, this new coating can inhibit the crack formation and enhance the corrosion protection of Ti. The in vitro bioactivity of the samples reveals that the presence of GO fillers promotes the bioactivity and cell proliferation.

Rad et al. [61] investigated the effects of the EPD at dynamic voltage on the biological and physical properties of HA coatings on pure Ti substrates. The voltages of 10 V, 20 V, 40 V, and 80 V were applied, and the corresponding damping currents were attained as 0.07 mA, 0.15 mA, 0.25 mA, and 0.35 mA. Figure 13 exhibits the surface morphology of coated samples obtained at different damping currents, and views of their cross sections.
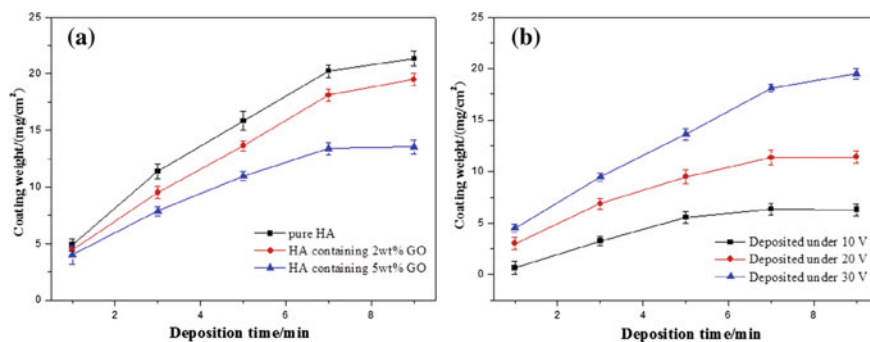
Fig. 12 The coating weight versus deposition time with various GO concentrations at voltage of 30 V (**a**), and with 2 wt.% GO at different voltage (**b**). Reprinted from Li et al. [60], with permission from Elsevier. Copyright (2014)

At higher voltages, the HA particles begin to accumulate in a more porous structure. The samples attained at 40 and 80 V showed highly porous, cracked, and non-stable coating. The optimum results were found at 20 V. The corrosion studies were done in Ringer's solution. The coated samples showed more resistance to corrosion relative to the uncoated sample. The biological experiments were performed by MG63 cells cultured on HA-coated samples. The number of cells attached to the sample increased with longer incubation time. The MG63 cells enlarge on the HA-coated and uncoated specimens after 72 h. The cells on the HA sample proliferate over the coating material and grow more efficiently on the substrate. The cells on the uncoated sample depict a flattened and osteoblast-like morphology.

Mehboob et al. [62] investigated polyethylene glycol (PEG) coated HA coatings on 316L SS via EPD. DC power supply was regulated at 30 V for 2 min. The amount of PEG in HA suspension was in different HA:PEG ratios; 1:0.1, 1:0.2, 1:0.5, and 1:1. Uniform coverage and increased adhesion to substrate was achieved in the case of 1:1 HA:PEG ratio. PEG was used to enhance the binding strength and packing density between coating and substrate. It was found that as the potential difference across the electrodes was constant, the electric field affecting electrophoresis reduced with time due to deposition of ceramic particles on the electrode, which acts as an insulating layer for the incoming particles. The incorporation of PEG improved the coating adhesion, and exhibited greater degree of packing density, which will potentially induce osteointegration of the implants with the living tissues of human.

Janković et al. [63] evaluated the HA and graphene (HA-Gr) composite coating done by EPD on Ti to attain a uniform coating with enhanced corrosion stability in SBF. The corrosion resistance of HA-Gr and HA coatings was determined by electrochemical impedance spectroscopy (EIS) measurements. On the basis of EIS data, it was apparent that the HA-Gr composite coating revealed biomimetic mineralization preeminent to its pure HA counterpart, and increased precipitation of a newly developed apatite layer.
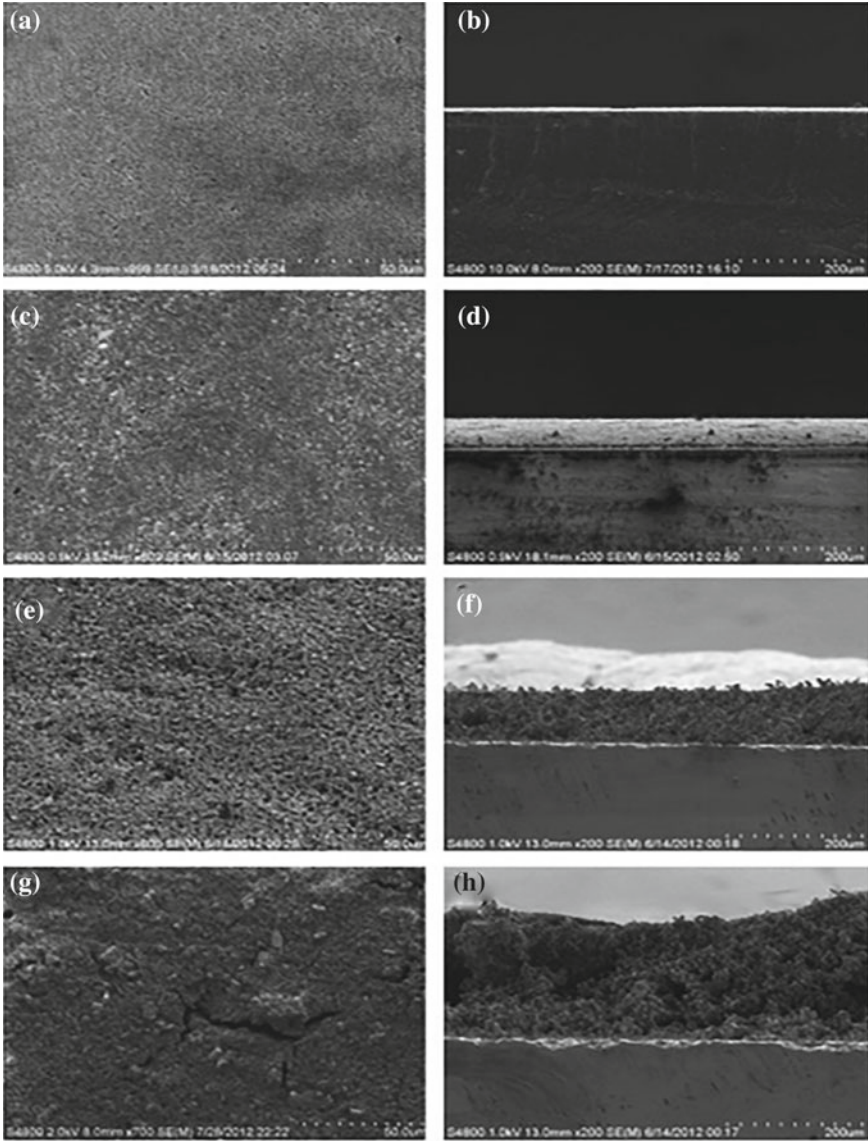
Fig. 13 SEM and the corresponding cross-sectional images of HA coatings on Ti substrates obtained using EPD process at dynamic voltage-constant current, **a**, **b** 0.07 mA, **c**, **d** 0.15 mA, **e**, **f** 0.25 mA, and **g**, **h** 0.35 mA. Reprinted from Rad et al. [61], with permission from Elsevier. Copyright (2014)

Molaei et al. [64] illustrated EPD of chitosan-bioglass-hydroxyapatite (CS-BG-HA) coatings on the Ti substrate by examining the parameters such as pH, voltage, and deposition time. Figure 14 shows the relationship between deposited weight and thickness of coating versus pH values. The deposition was performed at various pH values of 3.3, 4.5, and 5.
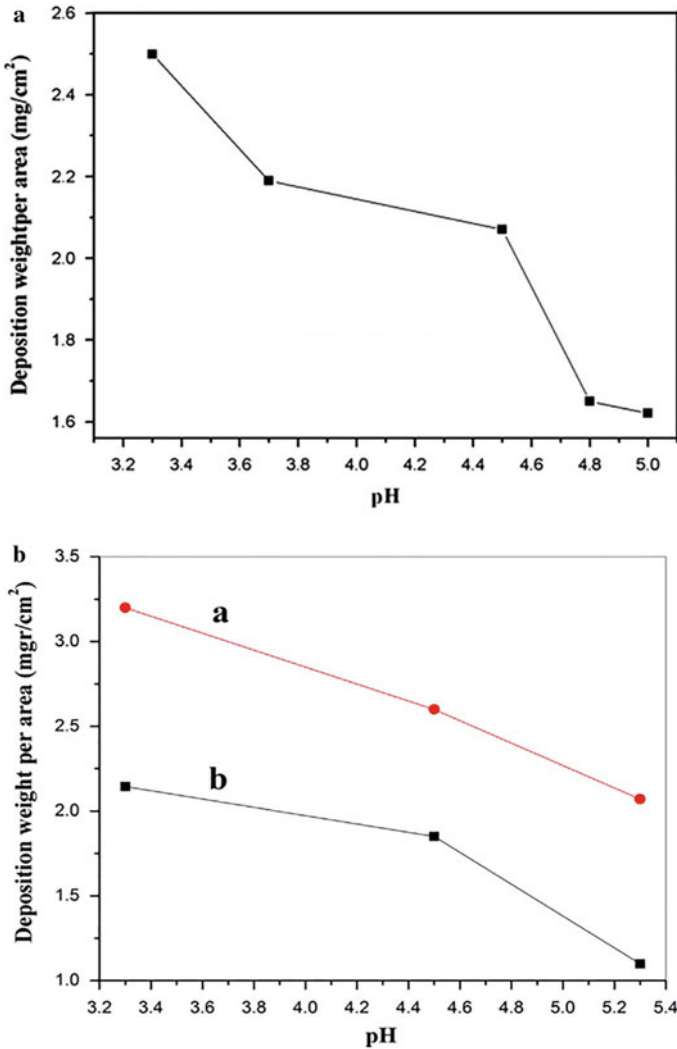
Fig. 14 **a** Deposition weight of CS-BG-HA coating at 30 V for 5 min, **b** variation of weight deposit of CS-BG-HA fabricated on (a) isolated and (b) non-isolated Ti at 20 V for 15 min. and **c** thickness of the CS-BG-HA fabricated on isolated Ti at 20 V for 15 min. All against pH of suspension used. Reprinted from Molaei et al. [64], with permission from Elsevier. Copyright (2015)
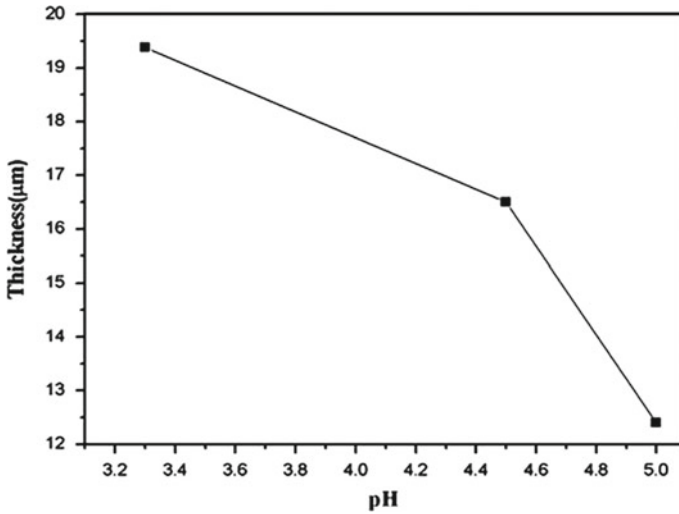
Fig. 14 (continued)

It was observed that deposited weight decrease at higher pH value due to its effect on zeta potential. In ethanol-based suspension, BG particles have higher zeta potential than particles of HA. Particles with larger zeta potential have higher mobility, so they travel quickly to the electrode of the opposite charge. Therefore, by decreasing pH, BG particles have higher rate of deposition, and corrosion resistance was improved. The sample formed at pH = 3.3 displayed the superior bioactivity and corrosion rate.

Razavi et al. [65] investigated the fluoridated hydroxyapatite (FHA) coating on AZ91 Mg by MAO and EPD to improve their corrosion through surface modifications. The electrochemical test was carried out with the help of the Potentiostat apparatus. The values of E_{corr} in samples were observed as follows: FHA coating $(-1.39 \text{ V}) > \text{MAO} (-1.56 \text{ V}) > \text{AZ91} (1.6 \text{ V})$ whereas the position of the I_{corr} value of FHA coating (12.5 nA/cm^2) was declined as compared to the MAO $(53,700 \text{ nA/cm}^2)$ and AZ91 $(63,100 \text{ nA/cm}^2)$. Therefore, the findings of E_{corr} and I_{corr} values indicated that the FHA-coated sample has a noticeably more corrosion ability than that of the MAO-coated samples.

Farnoush et al. [66] performed MAO on Ti to produce porous TiO_2 coatings retaining CaP. The MAO was performed at 300 V, 330 V, and 360 V for 5 min. The MAO treatment was done for providing an interlayer that improves the mismatch between titanium substrate and final coating. The electrochemical behavior and bonding strength were also enhanced. The EPD was done at 30 V for 120 s subsequently on the MAO substrate to deposit HA-BG composite coatings. The SEM images of samples after MAO at various voltages is displayed in Fig. 15. It can be seen that as the voltage rose to 360 V, the size of the HA clusters became larger and they connected to each other.
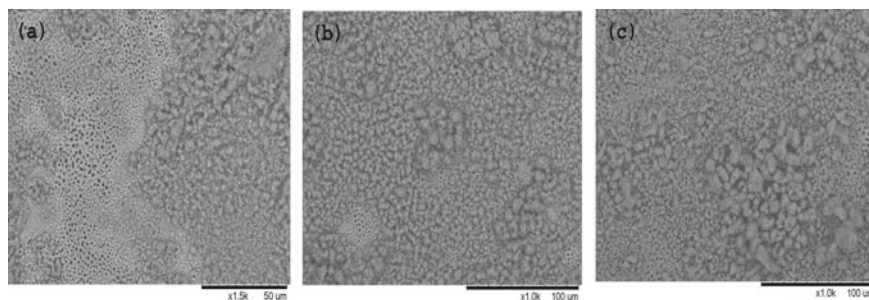
Fig. 15 SEM images of the MAO samples at **a** 300 V, **b** 330 V and **c** 360 V. Reprinted from Farnoush et al. [66], with permission from Elsevier. Copyright (2015)

The porous TiO_2 layer was completely encased with enlarged HA clusters due to the higher sparks and current density on the samples surface. Based on the electrochemical corrosion behavior of samples, the result of samples denoted by HA-BG-MAO 360 Ti and HA-MAO 360 Ti (where 360 refers to the voltage and Ti to the substrate) implies a significant decline in the current density, and increase in corrosion potential. The higher bonding strength was achieved with MAO. It helps in reducing the thermal expansion mismatch between substrate and coating, which results in higher densification.

Drevet et al. [67] studied the synthesis of HA coating by EPD of a nanosized powder. The influence of potential and deposition time variation on the corrosion behavior was explored. EPD was done in a suspension formulated by adding 2 g of HA nanopowder in 25 ml ethanol. The voltage was varying from 5 to 20 V and time from 5 to 20 min. The SEM micrographs obtained at different voltages are shown in Fig. 16.

At the higher voltage, and with the increase in time, the samples revealed cracks, and uncovered areas. These observations can be ascribed to particles agglomeration that progressively enhanced the surface electrical resistance, which can increase the corrosion rate in SBF. The best EPD conditions were obtained at 10 V for 10 min, which leads to compact and uniform coating.

Bakin et al. [68] produced Mg-substituted Cap coating on Ti-6Al-4V substrate for improving surface bioactivity and corrosion performance of coating. Four distinct solutions were made with various Mg contents of 0, 10, 20, and 40 (in wt.%). All coatings showed a needle-like morphology. The coating developed with 10% Mg content acquired the superior corrosion resistance relative to 20 and 40% addition of Mg. The samples were covered with apatite layer after immersion of 7 days. The surface morphology of coating transformed to spheres, and these spheres enclosed the whole surface completely. The surface of coatings becomes compact after 14 days of immersion and the formation of apatite distributed on the entire surface.

Molaei et al. [69] evaluated the effect on CS-BG-HA-halloysite (Hal) nanotube films by varying the concentration of halloysite on pure Ti. EPD was done in a solution containing 0.7 g/L HA, 0.6 g/L Hal, and 0.7 g/L BG in (17%) water–ethanol mixture,
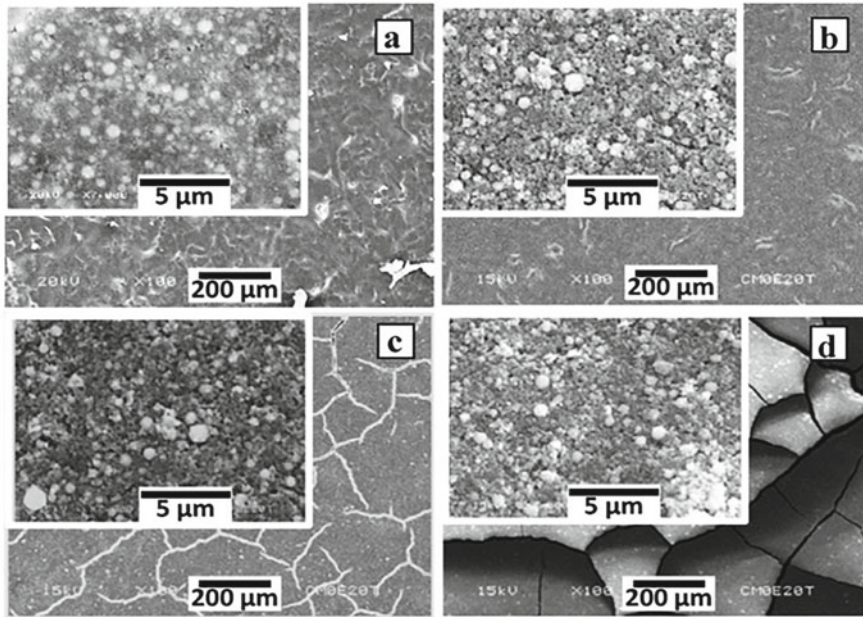
Fig. 16 SEM micrographs at low magnification and high magnification images (insets) for HA coatings attained in 10 min at **a** 5 V, **b** 10 V, **c** 15 V, and **d** 20 V. Reprinted from Drevet [67], with permissions from Elsevier. Copyright (2016)

because of fast sedimentation, whereas the dispersion was stable with (30%) water–ethanol solvent during 30 min. Hence, the desirable mixture for CS-BG-HA was chose 30% water–ethanol solvent as shown in Fig. 17.

The optimum pH chosen was in the range of 2.5 < pH < 3. From potentiodynamic polarization curves it was observed that a better corrosion resistance of CS-BG-HA-Hal coated substrate $E_{corr} = -0.507$ V and $I_{corr} = 0.56$ µA/cm^2) in SBF at 37 °C with respect to bare Ti ($E_{corr} = -587$ V and $I_{corr} = 91$ µA/cm^2).

Jugowiec et al. [70] reported EPD on Ti-13Nb-13Zr with chitosan (CS) coatings. The effect of the composition of colloidal solution and EPD variables on the performance of CS coatings was evaluated. The solution of CS (2 g/l) in a solution of distilled water and 0.5 vol % of acetic acid and 50 vol % of ethanol was employed for deposition. The voltage was varying from 5 to 30 V and the time (4 min) remained constant. It was observed that the coating uniformity is dependent on the composition of colloidal solution and stirring before EPD. The most homogenous coatings were deposited at a potential of 10 V and 4 min as shown in Fig. 18.

Kumar et al. [71] presented HA-coated Mg alloy via EPD. Corrosion behavior of the produced sample in the SBF solution was analyzed to recognize the potential of EPD deposited coating for orthopedic applications. The EPD was performed at 20 V for 10 min. It was observed that EPD deposited HA enhanced the corrosion protection of Mg alloy up to a magnificent 25 times. The penetration rate of Mg^{2+}
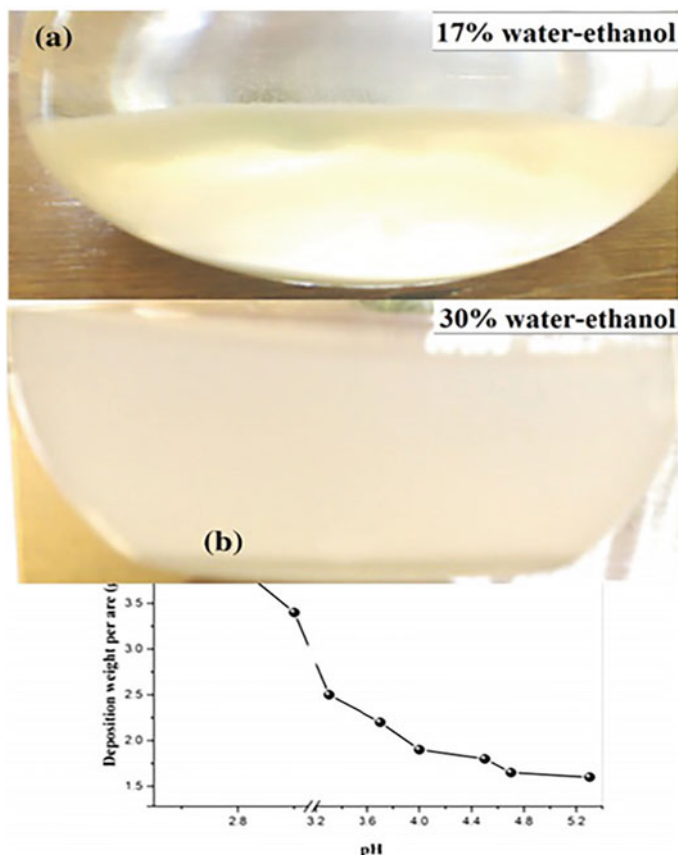
Fig. 17 a Digital image of dispersion having 17% water-ethanol (5 min) (**a**), and 30% water–ethanol (30 min). **b** The deposition weight as a function of pH produced from dispersion having 0.6 g/L Hal at 30 V. Reprinted from Molaei et al. [69], with permission from Elsevier. Copyright (2017)

ions in SBF for the coating with less roughness and more annealing temperature was small, implying the lowest degradation rate. The substantial increase in osteogenic cell adhesion was observed in the HA-coated Mg surface. Therefore, it has shown its potential to use for orthopedic implant applications.

Sankar et al. [72] compared the corrosion performance of HA-coated Mg, by employing two methods (a) EPD and (b) Pulsed laser deposition (PLD). By PLD, thin films were formed with the energetic condensation of atomic species. It efficiently forms highly adherent films. The layer of EPD coating was thick which leads to unstable behavior. The HA porous layer leads to more variation in the potential. Due to this, the corrosion rate of PLD-HA was 0.073 mm/yr, but of EPD-HA it was 0.194 mm/yr, and of the substrate it was 0.97 mm/yr. The adhesion of PLD-HA coating was observed to be 30% more as compared to that of the EPD-HA.
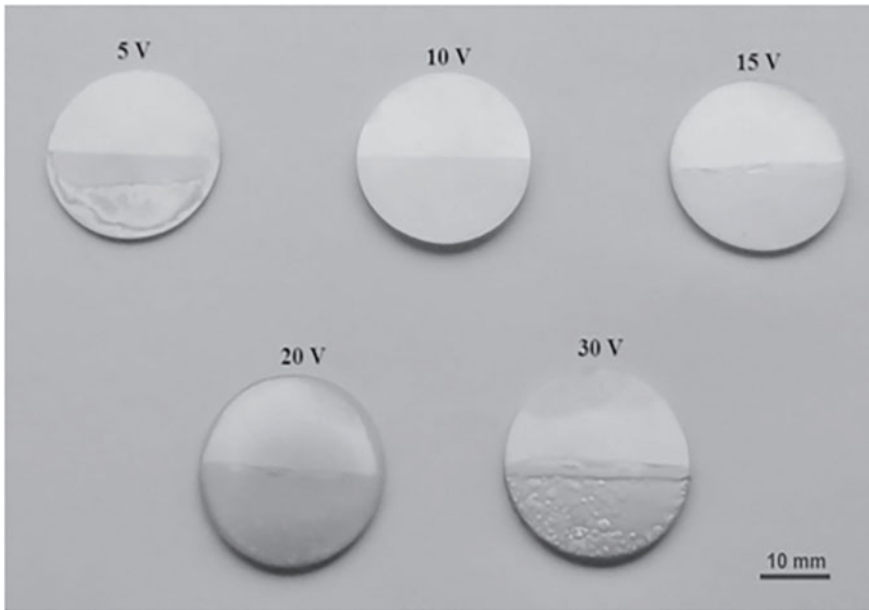
Fig. 18 Uncoated samples with 5–30 V and constant time of 4 min. Reprinted from Jugowiec et al. [70], with permission from Elsevier. Copyright (2017)

Huang et al. [73] investigated magnesium phosphate (MgP) and zinc phosphate (ZnP) doped HA composite coating deposited on AZ31 alloy by EPD. The corrosion behavior was observed through electrochemical tests and degradation tests. Pure HA, HA and MgP, HA and ZnP. HA, MgP, and ZnP coatings were plated with an electrochemical work station at room temperature. Compared with other samples, the electrochemical data showed that HA, MgP, and ZnP have the lowest I_{corr} value. The combination of HA, MgP, and ZnP proves great improvement in corrosion resistance for magnesium alloy.

Jugowiec et al. [74] deposited nanocomposite nc-CS/HA-p and nc-CS/HA-s coatings on Ti-13Nb-13Zr by EPD. The influence of HA particles in two different forms as nanopowder (p) and nanoparticles (s) on coating microstructure, adhesion and corrosion was investigated. Different suspensions of nc-HA-p (1, 2, 3, 4, 5 g/l) and nc-HA-s (4, 10, 15, 30 g/l) were formulated. EPD was carried out at 8–30 V for the time duration of 1, 2, 3, 4, 5, and 6 min. The homogeneous nc-CS/HA-s coatings were developed from 2 g/l of CS and 4 g/l of nc-HA-s suspension, at the potential of 10 V and 4 min as shown in Fig. 19. The formation of microcracks occurs at higher HA concentration in the nc-CS/HA-s coating. Moreover, the nc-CS/HA-s coating provides better adhesion and corrosion protection than the nc-CS/HA-p coating due to the absence of HA-s agglomerates.
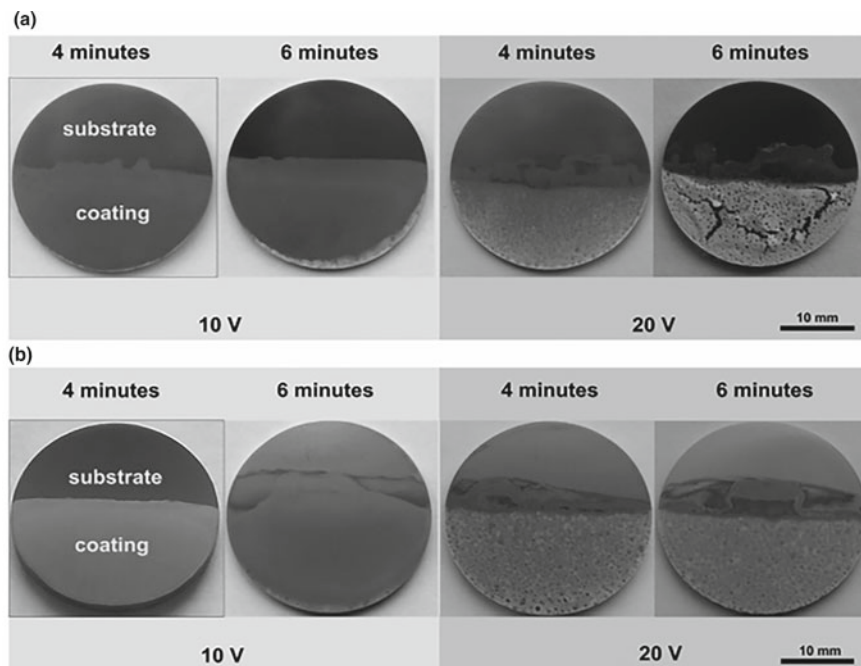
Fig. 19 Ti-13Nb-13Zr samples with **a** nc-HA-p/chitosan, and **b** nc-HA-s/chitosan. Reprinted from Jugowiec et al. [74], with permission from Elsevier. Copyright (2017)

Zhong and Ma [75] developed zinc substituted HA/silk fibroin (SF) coatings (HA-Zn-SF) on Ti by EPD. The SF has been widely explored to develop HA nanocomposite, which has similar structure relative to the natural bone minerals. The voltage and time duration were set as 30 V and 120 s. It was observed that the attained coatings were crack free and there was the excellent formation of apatite in SBF. The in vitro cell tests exhibited that the produced coatings offered good cytocompatibility.

Bartmanski et al. [76] examined the influence of EPD time on the coating homogeneity and the corrosion resistance. The electrochemical tests were conducted for all nano-HA coatings with nano-copper and reference Ti-13Zr-13Nb uncoated specimen. The Ti-13Zr-13Nb alloy was deposited with HA in a solution having 0.1, 0.2, or 0.5 g nano-HA in 100 mL of suspension and at 30 V for 1–2 min. Figure 20 illustrates the coatings derived at 1 min of EPD.

The coatings were inhomogeneous, and several HA agglomerates formed. The individual nano-HA layer, spheroidal nano Cu particles, passing through the HA layer were observed. Figure 21 presents the deposits obtained at 2 min. The HA agglomerates were increased in number due to the increase of time. The coating was more uniform relative to that deposited at 1 min. All nano-HA coatings had more noble corrosion potential than the uncoated sample.

Bakhsheshi-Rad et al. [77] prepared the TiO_2 incorporated MAO coatings (TM) on Mg-0.7Ca alloy. Afterward, zinc-doped hydroxyapatite (ZH) coating was formed
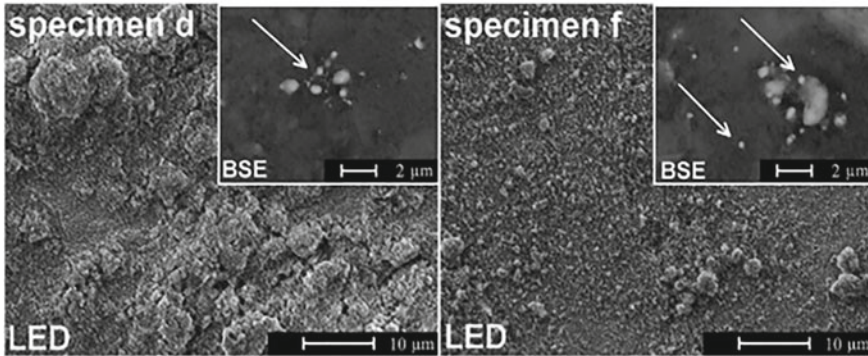
Fig. 20 Surfaces of d and f samples coated with (nano) HA and (nano) Cu at 1 min time on non-oxidized (left specimen d) and oxidized (right specimen f) titanium alloy. Nano Cu particles are indicated by arrows. Reprinted from Bartmanski et al. [76], with permission from Elsevier. Copyright (2019)
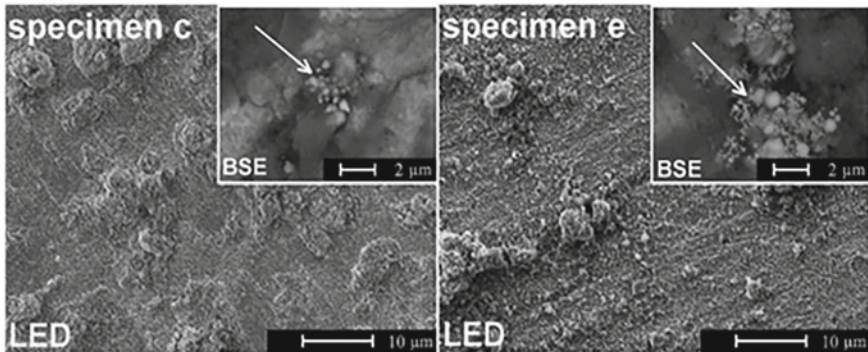
Fig. 21 Surfaces of c and e samples coated with (nano) HA and (nano) Cu coatings at 2 min time on non-oxidized (left specimen c) and oxidized (right specimen e) titanium alloy. Nano Cu particles are indicated by arrows. Reprinted from Bartmanski et al. [76], with permission from Elsevier. Copyright (2019)

by EPD on the MAO coating to reduce the Mg alloy degradation rate. The electrochemical test was conducted in SBF. The polarization plots revealed that cathodic and anodic branches transfer to lessen currents after coating. This may be ascribed to decreased solution diffusion into the substrate. The I_{corr} of Mg sample was detected to be (197.2 ± 8.1) $\mu A/cm^2$, while, after coating, the I_{corr} was declined to (9.8 ± 3.4) $\mu A/cm^2$. The ZH coating exhibited less I_{corr} (1.2 ± 0.3) $\mu A/cm^2$ than the TM coating, which was probably associated to the careful action of the top layer, by covering the TM film open pores. The E_{corr} of the TM coating was (-1600 ± 17) mV, which is about 65 mV more relative to the Mg substrate. After deposition of ZH,
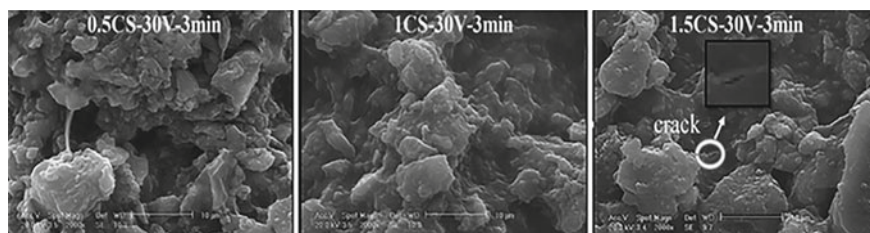
Fig. 22 SEM images of the CS-GO-HA coatings with different contents of chitosan, Reprinted from Karimi et al. [34], with permission from Elsevier. Copyright (2019)

the E_{corr} was moved to the positive position (-1520 ± 16) mV, and the corrosion rate was substantially inhibited.

Tozar and Karahan [78] investigated the single and integrated impacts of collagen (COL) and hexagonal boron nitride (h-BN) matrix on the corrosion performance and mechanical properties of HA-CS composite coatings. Collagen which is the primary human tissues ligament was employed as organic doped material owing to its perfect biodegradability and biocompatibility. The h-BN is a popular lubricant used as inorganic material for their excellent mechanical and corrosion properties. The EPD process was carried out with 15 V and 5 min duration. It was found that HA/CTS/COL/h-BN coatings can improve the mechanical properties and enhance the corrosion protection of Ti-6Al-4V alloys. The synergetic influence of collagen and h-BN in composite coating results in the formation of nucleation sites, which improves the bioactivity to a significant extent.

Karimi et al. [34] fabricated chitosan (CS) reinforced HA-graphene oxide (CS-GO-HA) nanocomposite coatings with different concentrations of CS (0.5, 1, and 1.5 mg/ml) by the EPD process to examine the effect of CS on the coating morphology. The EPD was performed at 30 V for 3 min. Figure 22 presents the SEM micrographs of CS-GO-HA coatings of different concentrations of chitosan.

The HA-GO nanoparticles were uniformly distributed over the entire surface of coatings. It was observed that the CS fills the pores among the interspaces of nanoparticles. However, an increment in the concentration of CS led to lower HA-GO nanoparticles deposition rate which may be due to the more electrolyte viscosity resulting in the lower mobility of particles. Mahmoodi et al. [79] documented an optimized viscosity concentration for obtaining the particles maximum deposition rate. In fact, an increase in the concentration of CS contributes to the microcracks formation, which can be seen in the sample denoted by (1.5CS-30V-3 min). It can be attributed to more absorption of water by enhancing the content of CS that could contribute to its evaporation process and resulting in coating crack formation. Of these coatings, the coating having 0.5 mg/ml CS showed I_{corr} of about 21 nA/cm^2 which was substantially less than the Ti with I_{corr} of 200 nA/cm^2.

Tayyaba et al. [80] synthesized HA coating using EPD on ZK60 Mg alloy. The degradation behavior of coatings has been compared with the Mg alloy in the Ringer's
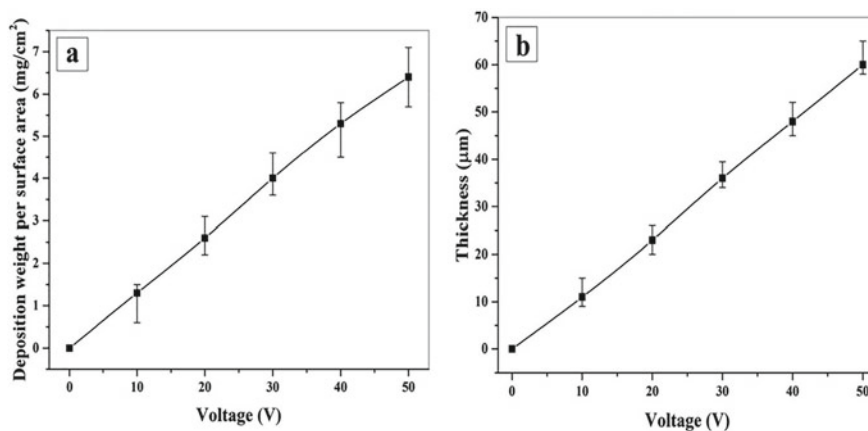
Fig. 23 **a** Deposition weight, and **b** coating thickness as functions of voltage in the range (10–50) V for 5 min. Reprinted from Molaei et al. [81], with permission from Elsevier. Copyright (2008)

solution (24–150) h. The DC power source was set at 100 V for 10 min. The electrochemical test revealed that the HA coatings were not degraded till 48 h and began to degrade at −1.8 V after immersion time of 72 h. The coatings were completely degraded in 128 h. The degradation rate of coated and uncoated samples was not significantly different after 150 h of immersion due to the $Mg(OH)_2$ precipitate formation on the coating surface. The 15 μm thick coating on ZK60 alloy declined the I_{corr} by one fold of magnitude and resulted in more than five times lower corrosion rate.

Molaei et al. [81] carried out EPD of CS-based nanocomposite coatings having BG, HA, and halloysite nanotubes (HNTs) on the Ti to study the effect of process variables such as voltage and deposition kinetics. The deposition was done at the (10–50) V with the duration of (5–25) min. Figure 23(a) and (b) shows the weight and thickness as functions of voltage.

As shown in Fig. 23, the deposition increases by increment in voltage. The lowest and highest deposition thickness and weight are developed from the suspension at 10 and 50 V. Such variations in the deposit thickness and weight are outcomes of the gap in the electric field strength. SEM images at various voltages are shown in Fig. 24. The result of Fig. 24(a) shows a thin film at 10 V. Owing to the lack of adequate force, there are no micro particles of BG in the coating. Figure 24(b) exhibits the coatings prepared at 30 V. The morphology of the composite shows that nano and micro particles were dispersed compactly and uniformly distributed throughout the CS matrix. In fact, increasing the voltage to 30 V ensures a uniform deposition with small cracks and porosity. When the voltage exceeds 50 V, the coating starts to deteriorate [Fig. 24(c)].

The explanation for this behavior is the creation of larger agglomerations and water electrolysis, because of the low voltage threshold. Coated sample produced at
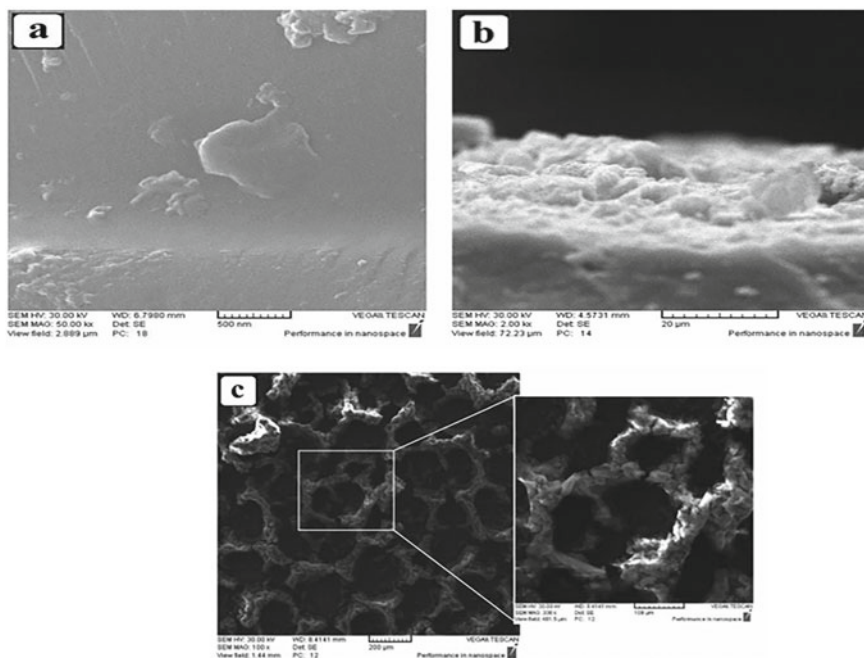
Fig. 24 SEM micrographs of CS-based coatings at **a** 10 V, **b** 30 V, and **c** 50 V. Reprinted from Molaei et al. [81], with permission from Elsevier. Copyright (2008)

30 V acquires excellent corrosion ability relative to the coated samples deposited at 10 and 50 V.

Ahmed et al. [82] obtained zein/HA coatings on Stainless steel (316L SS) via EPD. Zein/HA coatings need to be produced because they improve biocompatibility and corrosion resistance properties. EPD was conducted at voltages (6–15) V, and time duration (3–9) min. In an earlier study [83] it was demonstrated that the suspension becomes unstable, the HA particles concentration in suspension rises to 7.5 g/L and more voltages result in gas bubbles formation. Reportedly, the zein coatings developed at (3–5) V are very thin [84]. A better deposition of zein was obtained at 10 V. Figure 25 shows the SEM images of the zein/HA coatings (obtained at 15 V for 3 min duration, and HA concentration of 5 g/L). These parameters were found optimal during the deposition process.

The homogenous porous film on zein coating was observed. The HA particles are distributed homogeneously in the pores of the zein coating. The pores are blocked by the inclusion of agglomerated HA, which enhances the mechanical stability of the coating. Zein/HA coatings effectively increase the corrosion resistance of bare 316L SS. The coatings were bioactive upon immersion in SBF and the formation of HA crystals occurred after 3 days of immersion.

Antoniac et al. [85] examined the biodegradation rate of ZMX410 and ZM21 Mg alloys through HA coating via EPD. The corrosion rate (CR) of the Mg alloys are
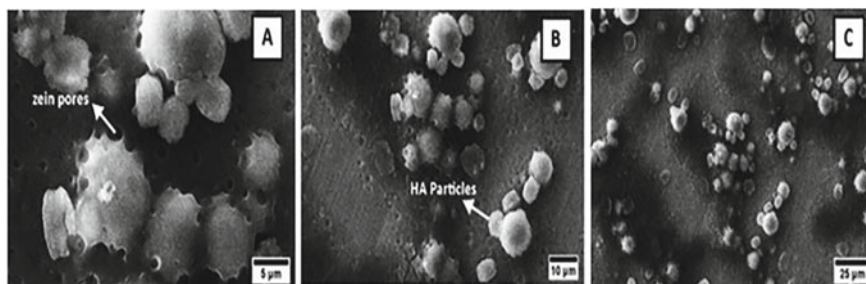
Fig. 25 SEM images of a zein/HA coating on Stainless steel (SS) substrate, (parameters: 5 g/L of HA, 3 min, 15 V); at different resolutions. Adapted from Ahmed et al. [82], under the terms and conditions of the Creative Commons Attribution (CC BY) license. (http://creativecommons.org/licenses/by/4.0/)

approximately equal, with the difference is 0.51 mm/year, in favor of the ZMX410 alloy. On the basis of efficiency toward corrosive attack, it was established that the coating with HA on ZM21 contributes by 40.6% to corrosion protection, and only 4.23% to the corrosion resistance in the ZMX410 alloy. Therefore, the degradation rate of both Mg alloys can be controlled by the EPD of HA coating.

4 Conclusion

The reviewed literature exhibited that EPD is an effective method for the processing of superior quality coatings. It was seen that a number of materials such as inorganic and organic–inorganic composite coatings can be developed in well-controlled manner. The HA-reinforced deposits showed improved characteristics including crack free films, oriented microstructures, enhanced corrosion resistance, and bioactivity properties. It was observed from the literature that the amount of deposit enhances with the increase in applied potential, but it leads to wrinkling, film roughness, and cracks in the coating. In addition, more deposition time results in insufficient attachment of coating to the base metal, and development of non-uniform and thick coatings. At high temperature, there were chances of cracking due to the difference in the sintered coating thermal expansion coefficients and the substrates. Therefore, a number of researchers employed different polymers as an effective binder to avoid the inconvenience of elevated temperature. Based on these findings, it may be concluded that a pilot study must be performed to optimize the parameters of EPD to obtain high quality, smooth, and homogeneous coatings. Furthermore, new experiments are to be conducted with the great potential of EPD for manipulation and assembly of HA composite coatings in which the effect of several other deposition parameters such as particle size, the dispersion medium, substrate, anode material, and temperature can be studied.

References

1. B. Ferrari, R. Moreno, J. Eur. Ceram. Soc. **30**(5), 1069 (2010)
2. O.O. Van der Biest, L.J. Vandeperre, Annu. Rev. Mater. Sci. **29**(1), 327 (1999)
3. L. Corni, M.P. Ryan, A.R. Boccaccini, J. Eur. Ceram. Soc. **28**(7), 1353 (2008)
4. Y. Ma, J. Han, M. Wang, X. Chen, S. Jia, J. Materiomics **4**(2), 108 (2018)
5. J. Kim, S.A. Guelcher, S. Garoff, J.L. Anderson, Adv. Coll. Interface. Sci. **96**(1–3), 131 (2002)
6. J.R. Woodard, A.J. Hilldore, S.K. Lan, C.J. Park, A.W. Morgan, J.A.C. Eurell, S.G. Clark, M.B. Wheeler, R.D. Jamison, A.J.W. Johnson, Biomaterials **28**(1), 45 (2007)
7. R. Ma, Y. Li, I. Zhitomirsky, JOM **62**(6), 72 (2010)
8. C.P. Klein, J.M.A. de Blieck-Hogemrst, J.G.C. Wolket, K. De Groot, Biomaterials **11**(7), 509 (1990)
9. R. Palanivelu, S. Kalainathan, A.R. Kumar, Ceram. Int. **40**(6), 7745 (2014)
10. P. Amaravathy, S. Sathyanarayanan, S. Sowndarya, N. Rajendran, Ceram. Int. **40**(5), 6617 (2014)
11. A. El-Ghannam, J. Biomed. Mater. Res. Part B: Appl. Biomater. **99**(2), 369 (2011)
12. S. Torgbo, P. Sukyai, Mater. Chem. Phys. **237**, 121868 (2019)
13. N. Saha, A.K. Dubey, B. Basu, J. Biomed. Mater. Res. Part B: Appl. Biomater. **100**(1), 256 (2012)
14. V.A. Thampi, B. Subramanian, J. Alloy. Compd. **649**, 1210 (2015)
15. D. Mishra, B. Bhunia, I. Banerjee, P. Datta, S. Dhara, T.K. Maiti, Mater. Sci. Eng. C **31**(7), 1295 (2011)
16. H. Sawalha, K. Schroën, R. Boom, J. Appl. Polym. Sci. **107**(1), 82 (2008)
17. J.G.P. Biner, *Advanced Ceramic Processing and Technology*, vol. 1, 1st ed. (Noyes Publications, 1990), pp. 255–283.
18. B. Ferrari, R. Moreno, J. Eur. Ceram. Soc. **17**(4), 549 (1997)
19. B. Ferrari, R. Moreno, Mater. Lett. **28**(4–6), 353 (1996)
20. M. Zarbov, I. Schuster, L. Gal-Or, J. Mater. Sci. **39**(3), 813 (2004)
21. J. Ervina, Z.A. Ghaleb, S. Hamdan, M. Mariatti, Compos. A Appl. Sci. Manuf. **117**, 1 (2019)
22. D.R. Brown, F.W. Salt, J. Appl. Chem. **15**(1), 40 (1965)
23. T. Mori, H. Nagashima, Y. Ito, Y. Era, J. Tsubaki, Miner. Eng. **133**, 119 (2019)
24. K. Hasegawa, S. Kunugi, M. Tatsumisago, T. Minami, J. Sol-Gel Sci. Technol. **15**(3), 243 (1999)
25. I. Zhitomirsky, L. Gal-Or, J. Mater. Sci. Mater. Med. **8**(4), 213 (1997)
26. R.N. Basu, C.A. Randall, M.J. Mayo, J. Am. Ceram. Soc. **84**(1), 33 (2001)
27. L. Sansone, V. Malachovska, P. La Manna, P. Musto, A. Borriello, G. De Luca, M. Giordano, Sens. Actuators, B Chem. **202**, 523 (2014)
28. V. Lee, L. Whittaker, C. Jaye, K.M. Baroudi, D.A. Fischer, S. Banerjee, Chem. Mater. **21**(16), 3905 (2009)
29. L. Besra, M. Liu, Prog. Mater. Sci. **52**(1), 1 (2007)
30. E. Tabesh, H.R. Salimijazi, M. Kharaziha, M. Mahmoudi, M. Hejazi, Surf. Coat. Technol. **364**, 239 (2019)
31. Y. Su, I. Zhitomirsky, Colloids Surf. A **436**, 97 (2013)
32. A.T. Koh, T. Chen, L. Pan, Z. Sun, D.H. Chua, J. Appl. Phys. **113**(17), 174909 (2013)
33. J. Du, Y. Zhang, S. Deng, N. Xu, Z. Xiao, J. Shi, Z. Wu, H. Cheng, Carbon **61**, 507 (2013)
34. N. Karimi, M. Kharaziha, K. Raeissi, Mater. Sci. Eng. C **98**, 140 (2019)
35. Y. Liu, D. Zhang, S. Pang, Y. Liu, Y. Shang, J. Sep. Sci. **38**(1), 157 (2015)
36. M. Diba, A. Garcia-Gallastegui, R.N.K. Taylor, F. Pishbin, M.P. Ryan, M.S. Shaffer, A.R. Boccaccini, Carbon **67**, 656 (2014)
37. P. Sarkar, P.S. Nicholson, J. Am. Ceram. Soc. **79**(8), 1987 (1996)
38. A. Aziz, S.A. Binti, S.H. Amirnordin, A. Hamimah, H.Z. Abdullah, H. Taib, Adv. Mater. Res. **488**, 1358 (2012)
39. W. He, L. Zhu, H. Chen, H. Nan, W. Li, H. Liu, Y. Wang, Appl. Surf. Sci. **279**, 416 (2013)

40. P. Subramanian, J. Niedziolka-Jonsson, A. Lesniewski, Q. Wang, M. Li, R. Boukherroub, S. Szunerits, J. Mater. Chem. A **2**(15), 5525 (2014)
41. M.S. Wu, Y.P. Lin, C.H. Lin, J.T. Lee, J. Mater. Chem. **22**(6), 2442 (2012)
42. R. Drevet, J. Fauré, H. Benhayoune, Adv. Eng. Mater. **14**(6), 377 (2012)
43. M. Dash, F. Chiellini, R.M. Ottenbrite, E. Chiellini, Prog. Polym. Sci. **36**(8), 981 (2011)
44. D. Stojanovic, B. Jokic, D. Veljovic, R. Petrovic, P.S. Uskokovic, D. Janackovic, J. Eur. Ceram. Soc. **27**(2–3), 1595 (2007)
45. A. Balamurugan, G. Balossier, G.J. Michel, J.M.F. Ferreira, Electrochim. Acta **54**(4), 1192 (2009)
46. D. Zhitomirsky, J.A. Roether, A.R. Boccaccini, I. Zhitomirsky, J. Mater. Process. Technol. **209**(4), 1853 (2009)
47. C.T. Kwok, P.K. Wong, F.T. Cheng, H.C. Man, Appl. Surf. Sci. **255**(13–14), 6736 (2009)
48. B. Zhang, C.T. Kwok, F.T. Cheng, H.C. Man, J. Nanosci. Nanotechnol. **11**(12), 10740 (2011)
49. Y. Bai, M.P. Neupane, I.S. Park, M.H. Lee, T.S. Bae, F. Watari, M. Uo, Mater. Sci. Eng. C **30**(7), 1043 (2010)
50. Y. Bai, K.A. Kim, I.S. Park, S.J. Lee, T.S. Bae, M.H. Lee, Mater. Sci. Eng. B **176**(15), 1213 (2011)
51. A.A. Abdeltawab, M.A. Shoeib, S.G. Mohamed, Surf. Coat. Technol. **206**(1), 43 (2011)
52. L. Mohan, D. Durgalakshmi, M. Geetha, T.S. Narayanan, R. Asokamani, Ceram. Int. **38**(4), 3435 (2012)
53. D. Sreekanth, N. Rameshbabu, Mater. Lett. **68**, 439 (2012)
54. H. Maleki-Ghaleh, V. Khalili, J. Khalil-Allafi, M. Javidi, Surf. Coat. Technol. **208**, 57 (2012)
55. R. Rojaee, M. Fathi, K. Raeissi, Appl. Surf. Sci. **285**, 664 (2013)
56. R. Rojaee, M. Fathi, K. Raeissi, IEEE Trans. Nanobiosci. **13**(4), 409 (2014)
57. S. Kaabi Falahieh Asl, S. Nemeth, M.J.T. Tan, *Paper presented at the 7th International Conference on Materials for Advanced Technologies (ICMAT 2013)*, Suntec City, Singapore, 30 June 2013 to 5 July 2013
58. Y. Huang, Q. Ding, S. Han, Y. Yan, X. Pang, J. Mater. Sci. Mater. Med. **24**(8), 1853 (2013)
59. H. Farnoush, A.A. Bastami, A. Sadeghi, J.A. Mohandesi, F. Moztarzadeh, J. Mech. Behav. Biomed. Mater. **20**, 90 (2013)
60. M. Li, Q. Liu, Z. Jia, X. Xu, Y. Cheng, Y. Zheng, T. Xi, S. Wei, Carbon **67**, 185 (2014)
61. A.T. Rad, M. Solati-Hashjin, N.A.A. Osman, S. Faghihi, Ceram. Int. **40**(8), 12681 (2014)
62. H. Mehboob, M. Awais, H. Khalid, S.A. Siddiqi, I. Rehman, Biomed. Eng. Appl. Basis Commun. **26**(6), 1450073 (2014)
63. A. Janković, S. Eraković, M. Mitrić, I.Z. Matić, Z.D. Juranić, G.C. Tsui, C.Y. Tang, V. Mišković-Stanković, K.Y. Rhee, S.J. Park, J. Alloy. Compd. **624**, 148 (2015)
64. A. Molaei, M. Yari, M.R. Afshar, Ceram. Int. **41**(10), 14537 (2015)
65. M. Razavi, M. Fathi, O. Savabi, D. Vashaee, L. Tayebi, Metall. Mater. Trans. A **46**(3), 1394 (2015)
66. H. Farnoush, F. Muhaffel, H. Cimenoglu, Appl. Surf. Sci. **324**, 765 (2015)
67. R. Drevet, N.B. Jaber, J. Fauré, A. Tara, A.B.C. Larbi, H. Benhayoune, Surf. Coat. Technol. **301**, 94 (2016)
68. B. Bakin, T.K. Delice, U. Tiric, I. Birlik, F.A. Azem, Surf. Coat. Technol. **301**, 29 (2016)
69. A. Molaei, M. Yari, M.R. Afshar, Appl. Clay Sci. **135**, 75 (2017)
70. D. Jugowiec, M. Kot, T. Moskalewicz, Arch. Metall. Mater. **61**(2), 657 (2016)
71. R.M. Kumar, K.K. Kuntal, S. Singh, P. Gupta, B. Bhushan, P. Gopinath, D. Lahiri, Surf. Coat. Technol. **287**, 82 (2016)
72. M. Sankar, S. Suwas, S. Balasubramanian, G. Manivasagam, Surf. Coat. Technol. **309**, 840 (2017)
73. W. Huang, B. Xu, W. Yang, K. Zhang, Y. Chen, X. Yin, Y. Liu, Z. Ni, F. Pei, Surf. Coat. Technol. **326**, 270 (2017)
74. D. Jugowiec, A. Łukaszczyk, Ł Cieniek, K. Kowalski, Ł Rumian, K. Pietryga, M. Kot, E. Pamuła, T. Moskalewicz, Surf. Coat. Technol. **324**, 64 (2017)
75. Z. Zhong, J. Ma, J. Biomater. Appl. **32**(3), 399 (2017)

76. M. Bartmanski, A. Zielinski, M. Jazdzewska, J. Głodowska, P. Kalka, Ceram. Int. **45**(16), 20002 (2019)
77. H.R. Bakhsheshi-Rad, E. Hamzah, A.F. Ismail, M. Aziz, M. Daroonparvar, E. Saebnoori, A. Chami, Surf. Coat. Technol. **334**, 450 (2018)
78. A. Tozar, İH. Karahan, Surf. Coat. Technol. **340**, 167 (2018)
79. S. Mahmoodi, L. Sorkhi, M. Farrokhi-Rad, T. Shahrabi, Surf. Coat. Technol. **216**, 106 (2013)
80. Q. Tayyaba, M. Shahzad, A.Q. Butt, M. Khan, A.H. Qureshi, Surf. Coat. Technol. **375**, 197 (2019)
81. A. Molaei, M. Lashgaroo, M. Yousefpour, J. Aust. Ceram. Soc. **56**(1), 1 (2020)
82. Y. Ahmed, M. Yasir, M.A. Ur Rehman, Surfaces **3**(2), 237 (2020)
83. H. Piri-Moghadam, M.N. Alam, J. Pawliszyn, Anal. Chim. Acta **984**, 42 (2017)
84. S. Kaya, A.R. Boccaccini, J. Coat. Technol. Res. **14**, 683 (2017)
85. I. Antoniac, F. Miculescu, C. Cotrut, A. Ficai, J.V. Rau, E. Grosu, A. Antoniac, C. Tecu, I. Cristescu, Materials **13**(2), 263 (2020)